UCRL-11781

University of California

Ernest O. Lawrence Radiation Laboratory

ELASTIC SCATTERING OF STRONGLY ABSORBED IONS

TWO-WEEK LOAN COPY

This is a Library Circulating Copy which may be borrowed for two weeks. For a personal retention copy, call Tech. Info. Division, Ext. 5545

Berkeley, California

DISCLAIMER

This document was prepared as an account of work sponsored by the United States Government. While this document is believed to contain correct information, neither the United States Government nor any agency thereof, nor the Regents of the University of California, nor any of their employees, makes any warranty, express or implied, or assumes any legal responsibility for the accuracy, completeness, or usefulness of any information, apparatus, product, or process disclosed, or represents that its use would not infringe privately owned rights. Reference herein to any specific commercial product, process, or service by its trade name, trademark, manufacturer, or otherwise, does not necessarily constitute or imply its endorsement, recommendation, or favoring by the United States Government or any agency thereof, or the Regents of the University of California. The views and opinions of authors expressed herein do not necessarily state or reflect those of the United States Government or any agency thereof or the Regents of the University of California.

UNIVERSITY OF CALIFORNIA
Lawrence Radiation Laboratory
Berkeley, California

AEC Contract No. W-7405-eng-48

ELASTIC SCATTERING OF STRONGLY ABSORBED IONS

Evangelos Hadjimichael
(Ph. D. Thesis)

April 8, 1965

ELASTIC SCATTERING OF STRONGLY ABSORBED IONS

Contents

Abstract v

I. Introduction 1

II. Theory and Method of Analysis

A. Relevant Formulas 4

B. The "Sharp Cutoff" Model 5

C. Modified "Sharp Cutoff" Model 6

D. Analytical Methods 8

E. A Model for Phase-Shift Analysis 11

F. Data Analysis 19

III. Experimental Procedure

A. Objective 22

B. Apparatus 22

IV. Experimental Results and Theoretical Analysis

A. Elastic Scattering. 32

B. Inelastic Scattering 93

C. Applicability of the Diffraction Model in the Elastic $\pi^{\pm}p$ Scattering at very High Energies and Nonforward Angles 98

Acknowledgments 102

References 103

ELASTIC SCATTERING OF STRONGLY ABSORBED IONS

Evangelos Hadjimichael

Lawrence Radiation Laboratory
University of California
Berkeley, California

April 8, 1965

ABSTRACT

The interaction radius R and the nuclear surface thickness ΔR of several nuclei have been investigated by phase-shift analysis of elastically scattered strongly absorbed ions. For the analysis, a diffraction model is used which was first proposed in a simple form by Blair, and was later modified by McIntyre et al. It is further modified in the present work to account for physical arguments that suggest a particular functional form for the nuclear phase shift and the partial-wave scattering amplitude as functions of the angular momentum.

The elastic scattering of C^{12} and O^{16} ions has been measured as a function of angle by using the Berkeley heavy-ion linear accelerator (Hilac). In addition, existing data were analyzed on elastic scattering of α particles, He^3 ions, and deuterons at several energies. Unambiguous parameters were obtained from which the nuclear radius $R_n \approx r_a A^{1/3}$ and the nuclear surface thickness ΔR were calculated. It was found that $\Delta R \approx 1.6 \times 10^{-13}$ cm and the radius parameter $r_a \approx 1.398 \times 10^{-13}$ cm. The total reaction cross sections were also calculated. A comparison with results obtained by other methods is presented. Finally, the versatility and validity of the present model in the region of relativistic energies is demonstrated by its successful application to the $\pi^- p$ elastic scattering at 2.01 BeV.

I. INTRODUCTION

Strong absorption of incident ions by target nuclei is characterized by a rapid drop of the intensity of the wave that describes the ion, within the nuclear dimensions of the target. Elastic scattering in the presence of strong absorption results in an angular distribution of the diffraction type. This is due to the total or partial removal (absorption) from the incident channel of several partial waves, and the interference among the rest. Nuclear scattering data for charged particles presented in the form

$$\sigma/\sigma_R = \frac{(\text{Differential elastic scattering cross section})_{c.m.}}{\text{Rutherford cross section}}$$

may be classified according to one of the three curves shown in Fig. 1.:[1] (a) large oscillations (Al curve), (b) a drop in the cross section with oscillations (Ag curve), (c) a smooth drop in the cross section (Ta curve). It has been observed that the parameter primarily responsible for the angular form of σ/σ_R is the Coulomb-interaction strength parameter $n = Z_1 Z_2 e^2/\hbar v$, where $Z_1 e$ and $Z_2 e$ are the charges of the incident ion and the target nucleus respectively, and v is the relative velocity between the two particles.[2] Specifically, the transition from the curve with oscillations to that with the smooth drop-off occurs for values of n in the neighborhood of five for α-particle scattering.[3]

The present analysis is confined to the scattering of incident particles that exhibit a classical character, such as heavy ions, α particles, and even He^3 ions and deuterons at suitable energies. By classical character is meant that the wave packet is small compared to some characteristic nuclear dimension. If this dimension is half the classical distance of "closest approach" for a head-on collision, $R = Z_1 Z_2 e^2/2E$, where E is the center-of-mass energy, then R must be much greater than λ or R/λ must be much greater than 1. This may be written as

$$\frac{R}{\lambda\!\!\!^{-}} = \frac{Z_1 Z_2 e^2}{2\left(\frac{\hbar^2 k^2}{2m}\right)\left(\frac{1}{k}\right)} = \frac{Z_1 Z_2 e^2}{\hbar v} = n \gg 1 \quad . \tag{1}$$

Thus $n \gg 1$ guarantees that the collision is classical in nature to the effect that Coulomb orbits can still be assumed for the interacting particles. Consequently, the interaction radii and the nuclear surface thickness can

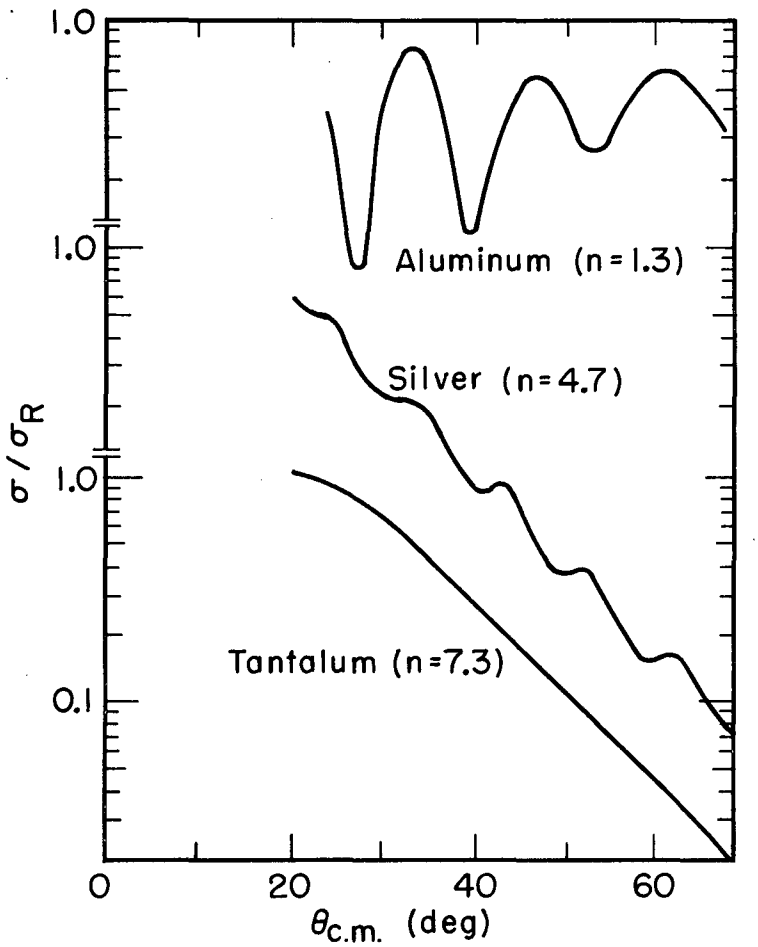

MU-35036

Fig. 1. Typical angular forms of the function σ/σ_R for the elastic scattering of charged particles; the three curves represent the angular distribution of 40-MeV α particles scattered elastically from Al, Ag, and Ta.

be determined accurately. In the results described here, n ranges from 10 to 30 for heavy ions, from 1 to 10 for α particles, and from 1 to 5 for He^3 ions and deuterons.

A second fact related to the classical nature of interactions with $n \gg 1$ is that a very high number of angular momenta are involved. This allows localization in space of the scattered particles. For example, in the scattering of C^{12} ions from Ta^{181}, orbital angular momenta of 90 $\hbar$ may be important.

Finally, in this work spin-flip scattering and generally the effects of a possible spin-orbit force are assumed to be unimportant in the analysis of the differential-cross-section data.

II. THEORY AND METHOD OF ANALYSIS

A. Relevant Formulas

The differential cross section in the center-of-mass (c.m.) system is given by[4]

$$\sigma(\theta) = |f(\theta)|^2 \quad , \tag{2}$$

where the scattering amplitude, $f(\theta)$, in terms of partial waves is

$$f(\theta) = \frac{-1}{2ik} \sum_{\ell=0}^{\infty} (2\ell+1)\,(1-\eta_\ell)\,P_\ell(\cos\theta) \quad . \tag{3}$$

Here k is the wave number in cm^{-1} in the c.m. system, ℓ is the orbital-angular-momentum quantum number, and η_ℓ is the amplitude of the ℓth outgoing partial wave. We formally write $\eta_\ell = \exp(2i\delta_\ell)$. The unitary condition requires that $|\eta_\ell| \leq 1$. In the case of absorptive scattering, the phase shift is complex, $\Delta_\ell = \delta_\ell + i\beta_\ell$. The condition $|\eta_\ell| \leq 1$ necessitates that β_ℓ is never negative. Let us write

$$\eta_\ell = \exp[2i(\delta_\ell + i\beta_\ell)] = \exp(-2\beta_\ell)\exp(2i\delta_\ell) = A_\ell \exp(2i\delta_\ell) \quad . \tag{4}$$

Then we have $|\eta_\ell| = A_\ell \leq 1$. The real part δ_ℓ is the phase shift due to the interacting potential; A_ℓ is a measure of absorption and henceforth, is referred to as an absorption amplitude. To take into account the Coulomb interaction we add the Coulomb phase shift, $\sigma_\ell = \arg\Gamma(1+\ell+in)$,

$$\eta_\ell = A_\ell \exp[2i(\sigma_\ell + \delta_\ell)] \quad . \tag{5}$$

This leads to

$$\begin{aligned} f(\theta) &= \frac{-1}{2ik} \sum_{\ell=0}^{\infty} (2\ell+1) \left\{1 - A_\ell \exp[2i(\sigma_\ell+\delta_\ell)]\right\} P_\ell(\cos\theta) \\ &= \frac{i}{2k} \sum_{\ell=0}^{\infty} (2\ell+1)\,[1-\exp(2i\sigma_\ell)]\,P_\ell(\cos\theta) \\ &+ \frac{1}{2ik} \sum_{\ell=0}^{\infty} (2\ell+1)\exp(2i\sigma_\ell)\,[A_\ell \exp(2i\delta_\ell) - 1]\,P_\ell(\cos\theta) \\ &= f_c + f_n \quad . \end{aligned} \tag{6}$$

The first term is the partial-wave form of the Coulomb scattering amplitude,[4] and the second term is the nuclear scattering in the presence of absorption and Coulomb scatter. From Eqs. (2), (3), and (5) one obtains the total elastic cross section

$$\sigma_{e\ell} = \frac{\pi}{k^2} \sum_{\ell=0}^{\infty} (2\ell + 1) \left| 1 - \eta_\ell \right|^2 \tag{7}$$

and the total absorption cross section

$$\begin{aligned} \sigma_a &= \frac{\pi}{k^2} \sum_{\ell=0}^{\infty} (2\ell + 1) \left(1 - |\eta_\ell|^2\right) \\ &= \frac{\pi}{k^2} \sum_{\ell=0}^{\infty} (2\ell + 1) \left(1 - A_\ell^{\,2}\right) . \end{aligned} \tag{8}$$

B. The "Sharp Cutoff" Model

To explain experimental results on the scattering of α particles by heavy ions, J. S. Blair put forward a diffraction model with a crude semi-classical boundary condition at the nuclear surface.[5] The model assumes that (a) the target and the incident particle are considered as spheres of definite radii; (b) if the potential barrier for the ℓth wave allows the nucleus and the projectile to overlap when considered classically, the outgoing ℓth wave vanishes, i.e., is totally absorbed, thus contributing to the absorptive or "shadow" elastic scattering;[6] (c) if the barrier is such that the nucleus and projectile do not classically overlap, the outgoing ℓth wave undergoes pure Coulomb scattering. Mathematically these assumptions are

$$\begin{aligned} \eta_\ell &= 0 \quad \text{for} \quad \ell \leq \ell', \quad \text{because} \quad A_\ell = 0 \\ \eta_\ell &= \exp(2i\sigma_\ell) \quad \text{for} \quad \ell > \ell', \quad \text{because} \quad A_\ell = 1 \quad \text{and} \quad \delta_\ell = 0 . \end{aligned} \tag{9}$$

Evidently, ℓ' is the partial wave for which the distance of closest approach corresponds to the interaction radius R and is related to R by the semiclassical expression

$$E = \frac{Z_1 Z_2 e^2}{R} + \frac{\ell'(\ell'+1)\hbar^2}{2\,mR^2} . \tag{10}$$

Here E is the c.m. energy and m is the reduced mass. When the boundary conditions (9) are substituted into (6), one obtains

$$f(\theta) = \frac{1}{2ik}\sum_{\ell=0}^{\infty}(2\ell+1)\left[\exp(2i\sigma_\ell)-1\right]P_\ell(\cos\theta)+\frac{i}{2k}\sum_{\ell=0}^{\ell'}(2\ell+1)\exp(2i\sigma_\ell)P_\ell(\cos\theta). \tag{11}$$

Because of the sharp boundary condition (9), this model is generally known as the "sharp cutoff" model. As Blair has pointed out, the model does not allow either for absorption due to barrier penetration in the case of $\ell > \ell'$ or for reflection due to the change in the refractive index at the nuclear surface in the case of $\ell < \ell'$. Nondiffraction elastic scattering due to the nuclear potential is totally neglected, as evidenced by the absence of a nuclear phase shift δ_ℓ in Eq. (11). Figure 2 shows a typical fit to the experimental σ/σ_R for the elastic scattering of 48.2-MeV α particles from gold,[7,8] obtained with the sharp cutoff model. The calculated ratio σ/σ_R identifies fairly accurately the angle where $\sigma(\theta)$ breaks away from $\sigma_R(\theta)$; beyond that angle, σ/σ_R assumes an oscillatory form which is in complete disagreement with the experimental curve. The large oscillations are due to the sharp boundary condition. This is very characteristic of the sharp cutoff model.

C. Modified "Sharp Cutoff" Model

McIntyre et al. modified the Blair model as follows:[9] (a) They let the term A_ℓ that is indicative of absorption in the partial-scattering amplitude, vary smoothly with ℓ, from 0 to 1, over a range $\Delta\ell$. To accomplish this, they chose the arbitrary relationship

$$A_\ell = \left[1+\exp\left(\frac{\ell_A-\ell}{\Delta\ell_A}\right)\right]^{-1}. \tag{12}$$

(b) They introduced a real nuclear phase shift δ_ℓ, thus allowing for the fact that the nuclear potential contributes to the scattering. They also made δ_ℓ vary smoothly with ℓ through the arbitrary relationship

$$\delta_\ell = \delta\left[1+\exp\left(\frac{\ell-\ell_\delta}{\Delta\ell_\delta}\right)\right]^{-1} \tag{13}$$

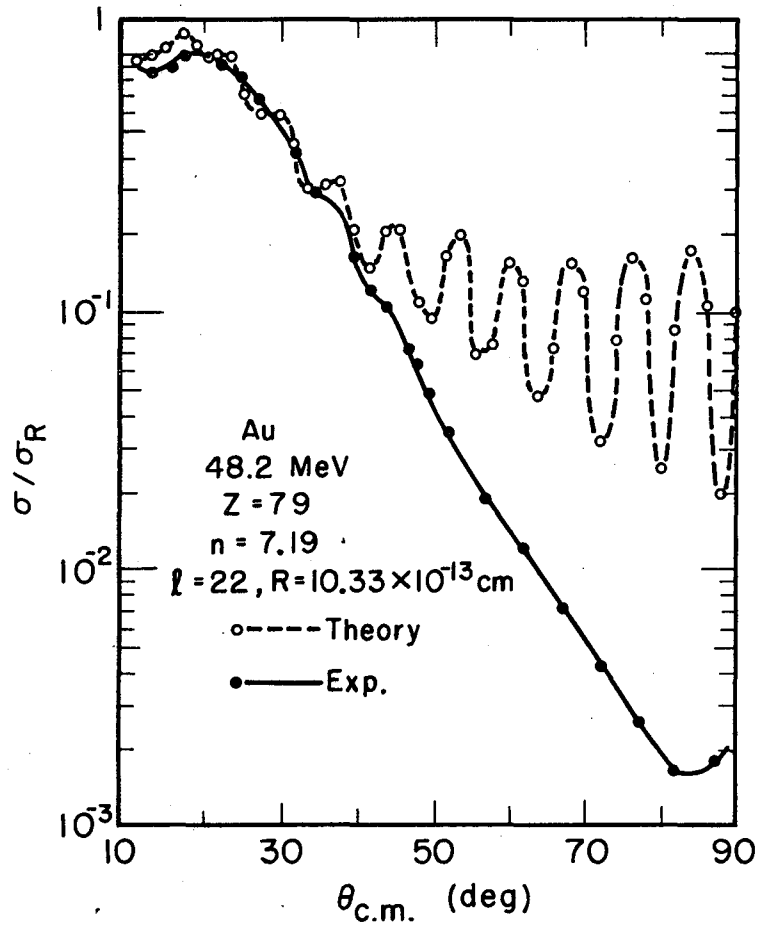

MU-35035

Fig. 2. σ/σ_R for 48.2-MeV α particles scattered from Au. The solid curve and dots represent the experimental data. The dotted curve and open circles represent the "sharp-cutoff" angular distribution for $\ell' = 22$, $R = 10.33 \times 10^{-13}$ cm.

where $\Delta\ell_A$ and $\Delta\ell_\delta$ determine the range of ℓ over which A_ℓ and δ_ℓ drop from their maximum to zero. The form of A_ℓ and δ_ℓ is shown graphically in Fig. 3. Using the known Coulomb amplitude, f_c, in the expression for σ/σ_R, one obtains

$$\frac{\sigma}{\sigma_R} = \left| - i \exp[-in(\ln \sin^2\theta/2)] - \frac{\sin^2\theta/2}{n} \sum_{\ell=0}^{\infty} [1 - A_\ell \exp(2i\delta_\ell)] \times (2\ell+1) P_\ell(\cos\theta) \exp[2i(\sigma_\ell - \sigma_0)] \right|^2 . \tag{14}$$

The Coulomb phase shift σ_ℓ is, of course, well known:

$$\sigma_\ell = \arg \Gamma(1+\ell+in) . \tag{15}$$

By using Eqs. (12), (13), and (14), McIntyre et al.[9] obtained a good fit to the experimental data Ag(α, α)Ag at 40 MeV. This is shown in Fig. 4, where curve (1) is obtained with the sharp cutoff model ($\Delta\ell_A = 0$, $\delta = 0$), curve (2) is obtained by introducing A_ℓ varying smoothly over a range proportional to $\Delta\ell_A(\delta = 0)$, and curve (3) is the one obtained when the full use of Eqs. (12) and (13) is made in Eq. (14). The parameters for curve (3) are $\ell_A = \ell_\delta = 19$, $\Delta\ell_A = 1.1$, $\Delta\ell_\delta = 1.6$, and $\delta = 0.3$.

Apparently, this contribution to the diffraction model seems to be successful at least in the case of α-particle scattering. However, two points must be made. First, the uniqueness of the parameters that yield curve (3) in Fig. 4 could not be verified. Second, forms (12) and (13) for A_ℓ and δ_ℓ were chosen quite arbitrarily. The five parameters ℓ_A, $\Delta\ell_A$, δ, ℓ_δ, and $\Delta\ell_\delta$ were given no physical significance, except perhaps for the correspondence between ℓ_A and the radius of interaction R through Eq. (10).

D. Analytical Methods

Taking advantage of the high number of partial waves involved in elastic scattering of strongly absorbed ions, and assuming that η_ℓ varies smoothly with ℓ, Greider and Glassgold[10] and recently Frahn and Venter[11] attempted to calculate $(d\sigma/d\Omega)_{c.m.}$ by approximate analytic methods. In particular, Frahn and Venter have parameterized

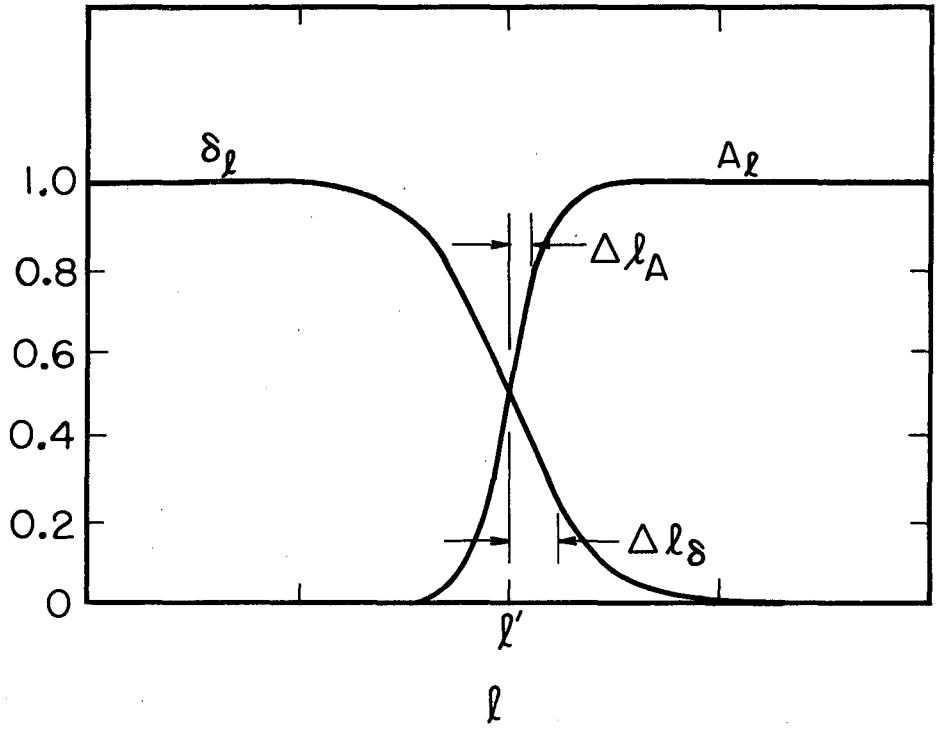

MU-35058

Fig. 3. Absorption amplutude and nuclear phase shift as functions of the angular momentum according to the modified sharp-cutoff model. The phase shift, δ_ℓ, is expressed in units of δ [see Eq. (13)].

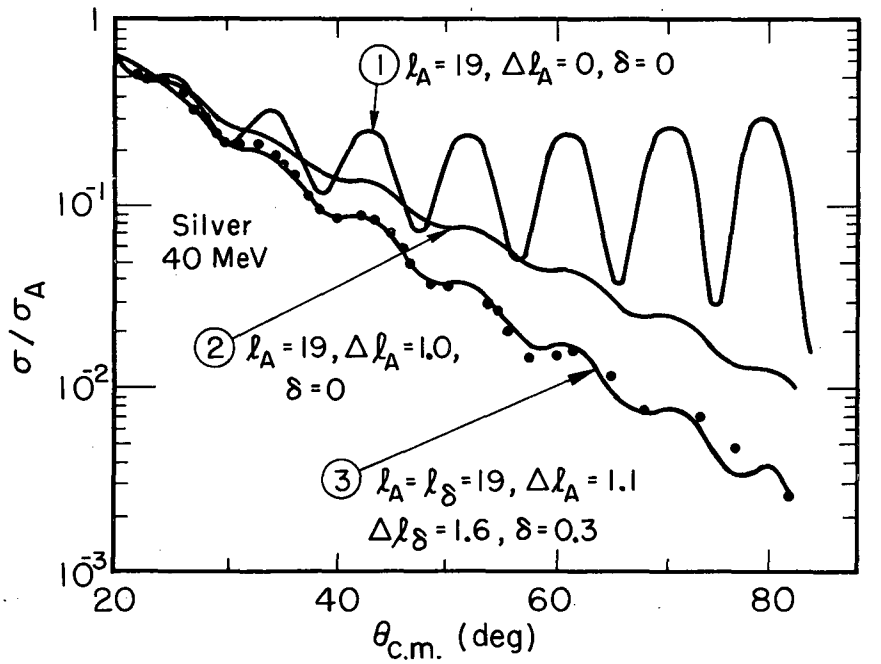

MU-35034

Fig. 4. The elastic scattering of 40-MeV α particles on gold. The dots are experimental points. Curve 1 is obtained with the sharp-cutoff model, curve 2 is obtained with the modified model and with $\delta = 0$, and curve 3 is obtained with $\ell_A = \ell\delta = 19$, $\Delta\ell_A = 1.1$, $\Delta\ell_\delta = 1.6$, and $\delta = 0.3$.

$\mathrm{Re}\eta_\ell$ and $\mathrm{Im}\eta_\ell$ separately; seven parameters have been used. The sum over partial waves in Eq. (3) has been replaced by an integral. Again, no physical significance was assigned the parameters. Furthermore, this model is limited to cases where the values of ℓ for which A_ℓ approaches 1 are sufficiently high. In other words when the value of ℓ at which A_ℓ approaches unity is only 4 or 5, then the sum over partial waves in (3) cannot be replaced by an integral.

E. A Model for Phase-Shift Analysis

In the present work an attempt is made to put the parameterized phase-shift analysis of the elastic-scattering data on a physical basis. Physical reasons are sought that prescribe a definite shape for the absorption amplitude A_ℓ and the real nuclear phase shift δ_ℓ.

1. A_ℓ

It has been mentioned previously that the unitarity condition on the partial scattering amplitude dictates that $0 \leq A_\ell \leq 1$. An examination of the total reaction cross section indicates which partial waves should have $A_\ell = 0$, or $0 < A_\ell < 1$ or $A_\ell = 1$. Let us rewrite here the total absorption cross section:

$$\sigma_a = \frac{\pi}{k^2} \sum_{\ell=0}^{\infty} (2\ell + 1)\,(1 - A_\ell{}^2) \quad . \tag{8}$$

A partial wave with a probability for absorption equal to 100% contributes a maximum amount to σ_a. This fact demands that $A_\ell = 0$, as seen from Eq. (8). To this category belong the partial waves with small angular-momentum quantum numbers, which represent incident particles with distances of closest approach [calculated from Eq. (10)] smaller than the nuclear radius. Incidentally, these waves each contribute an amount $(\pi/k^2)\,(2\ell + 1)$ to the total elastic-scattering cross section. As noted above, this is purely "shadow" elastic scattering. On the other hand, a partial wave with zero probability for absorption, does not contribute at all to σ_a. This fact necessitates that A_ℓ equal 1. To this category belong the partial waves with larger angular momentum

quantum numbers, that describe incident particles with distances of closest approach larger than the nuclear radius. The sharp-cutoff model assumes that there is a sharp dividing line between these two categories of partial waves, as shown in Fig. 5(a). The modified sharp-cutoff model has postulated a smooth transition $\Delta\ell$ from the partial waves with $A_\ell = 0$ to those with $A_\ell = 1$ [Figs. 3 and 5(b)]. Physically this indicates the existence of partial waves with a probability for absorption between zero and 100%. Empirically, the McIntyre assumption for a smooth transition is certainly favored, excluding all interactions of the resonant type where one or more partial waves are involved (see Fig. 4).[12]

The question to be answered now is what are the physical grounds for the existence of the smooth transition region. It is postulated here that this region is due to the existence of a nuclear surface where the nuclear mass density is gradually reduced from its maximum value at the nuclear core to zero, as the electron experiments of Hofstadter et al. have indicated.[13] Coulomb excitation is the only "at-a-distance" interaction that leads to an inelastic channel. All other absorptive processes, direct or otherwise, require that the interacting particles be in very close proximity. Note that all the cases studied below involve incident energies higher than the nuclear Coulomb barrier. Consequently penetration of the target nucleus by the projectile is possible, in which case the absorptive processes would reflect the spatial distribution of nuclear matter in the region where they occur. Consider a Woods-Saxon-type nuclear-density distribution and the classical Coulomb orbit of an incident particle that barely grazes the target nucleus. At this position the incident particle is close to one or more outlying nucleons. This opens up inelastic channels and results in a reduction of A_ℓ to values of less than 1. Incident particles that penetrate slightly deeper into the nuclear surface encounter increasingly dense nuclear matter and consequently more inelastic channels become available to them. The result is that A_ℓ quickly goes to zero. On the basis of this qualitative description, it is postulated that (a) the interaction radius R calculated from Eq. (10), approximately corresponds to that partial wave, $\ell = \ell_m$, which has $A_\ell = 1/2$,

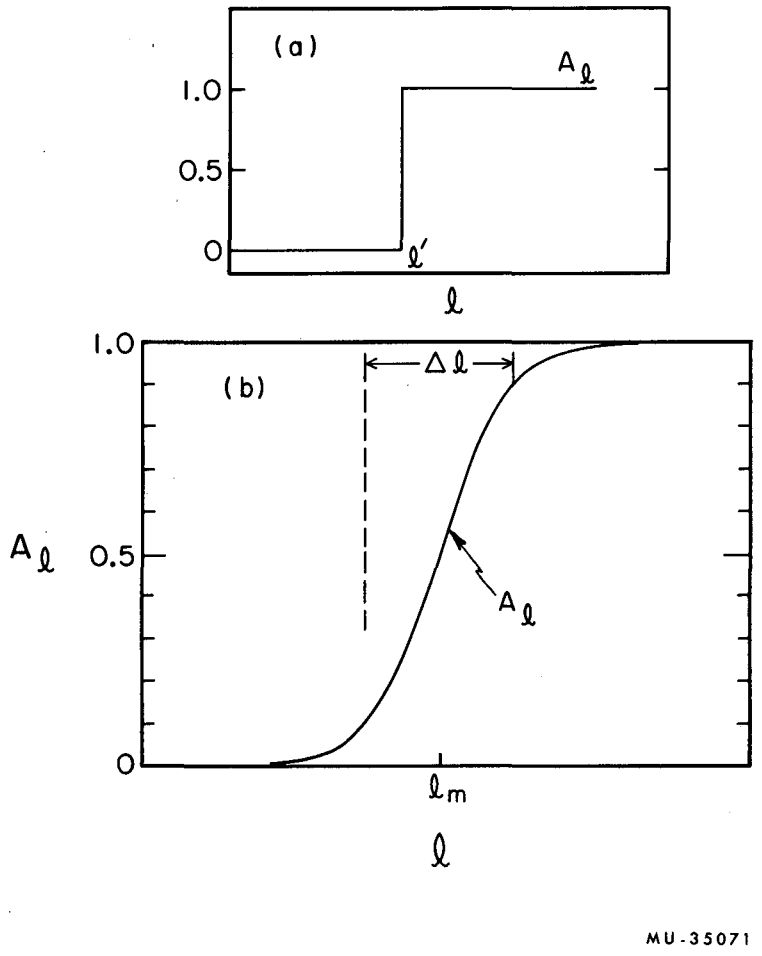

Fig. 5. (a) Absorption amplitude A_ℓ according to the sharp-cutoff model.

(b) Absorption amplitude, A_ℓ, plotted against ℓ, according to the modified sharp-cutoff model and the model employed in the present work.

i.e. an absorption probability equal to 50%. Equation (10) in terms of ℓ_m is rewritten

$$\hbar^2 \ell_m(\ell_m + 1) = 2m R^2 \left(E - \frac{Z_1 Z_2 e^2}{R}\right) . \qquad (10')$$

(b) The nuclear surface thickness is semiclassically related to the transition region $\Delta\ell$, by differentiating Eq. (10').

We obtain

$$\frac{\hbar^2(2\ell_m + 1)\Delta\ell}{2mR^2} = \left(2E - \frac{Z_1 Z_2 e^2}{R}\right) \frac{\Delta R}{R} . \qquad (16)$$

A functional form that satisfies the qualitative-requirements presented above is

$$A = \left[1 + \exp\left(\frac{\ell_m - \ell}{\Delta\ell_A}\right)\right]^{-1} . \qquad (17)$$

Defining $\Delta\ell$ as the region over which A_ℓ goes from 10% to about 90% of its maximum value as shown in Fig. 5(b), we obtain the relationship

$$\Delta\ell = 4.4\ \Delta\ell_A . \qquad (18)$$

This form of A_ℓ was adopted by McIntyre.

2. $\underline{\delta_\ell}$

There are qualitative arguments that prescribe the shape of the nuclear phase shift,[14] as well. It is expected that in going from large to small partial waves, δ_ℓ becomes increasingly more positive due to the attractive nuclear forces. As soon as absorption becomes operative, however, A_ℓ goes quickly to zero. Absorption also causes the real nuclear phase shifts to decrease and eventually become negative. That a connection exists between reactions and elastic scattering through the nuclear phase shifts is certainly nothing new. Morinigo proposed as much, and was able to obtain analytical expressions for the real and imaginary part of the nuclear phase shifts as a function of energy after he had subtracted the anomalies due to reactions.[15] Furthermore, Porter used the optical model,[16] where absorption is incorporated in the analysis by means of an imaginary part of the

nuclear potential, to examine the relationship between the absorptive part of the potential and the real nuclear phase shifts. Machine calculations were performed in the case of $N^{14} - N^{14}$ scattering. It was found that upon increasing the magnitude of the absorptive potential, the real phase shift as a function of the angular-momentum quantum number ℓ decreased and became negative for small ℓ. This is shown in Fig. 6, a and b, taken from Ref. 16. It has been stated previously that $\exp(-2\ \mathrm{Im}\delta_\ell) = A_\ell$. Moreover comparison of Figs. 7, a and b (Ref. 16) indicates that the phase shifts change with incident energy in a way that favors the assumption made here. For low energies when the absorption is not too great, the phase shift is positive. As the energy increases and the absorption becomes stronger, the phase shift becomes negative for small angular momenta.

In conclusion, the functional form of δ_ℓ should take into account the competitive effects of an attractive nuclear potential and of the absorption. A mathematical expression that allows for such considerations as were presented above is

$$\delta_\ell = \left[\delta_0 - \exp\left(\frac{\ell_m - \ell}{\Delta\ell'_\delta}\right)\right] \exp\left(\frac{\ell_m - \ell}{\Delta\ell_\delta}\right) . \tag{19}$$

Equation (19) involves four parameters, of which ℓ_m is the one that appears in the expression for A_ℓ. Figure 8 shows a plot of δ_ℓ vs ℓ. The $\Delta\ell'_\delta$ controls the slope of the left side of δ_ℓ. This is the region in the ℓ-space where absorption is prevailing and, consequently, $\Delta\ell'_\delta$ is primarily absorption-dependent. The $\Delta\ell_\delta$ controls the slope of the right side of δ_ℓ. This is the region where the attractive nuclear potential is predominant, and $\Delta\ell_\delta$ should reflect this fact. The magnitude of the phase shift at $\ell = \ell_m$, where $A_\ell = 1/2$, is $(\delta_0 - 1)$.

It must be made clear at this point that the nuclear phase shifts δ_ℓ obtained when the above parameterization is used to obtain fits to the experimental data are the phase shifts in the presence of Coulomb potential and, consequently, are the phase shifts relative to pure Coulomb-scattered waves.

For the calculation of σ/σ_R, Eq. (14) is again employed, with A_ℓ and δ_ℓ as given by Eqs. (17) and (19).

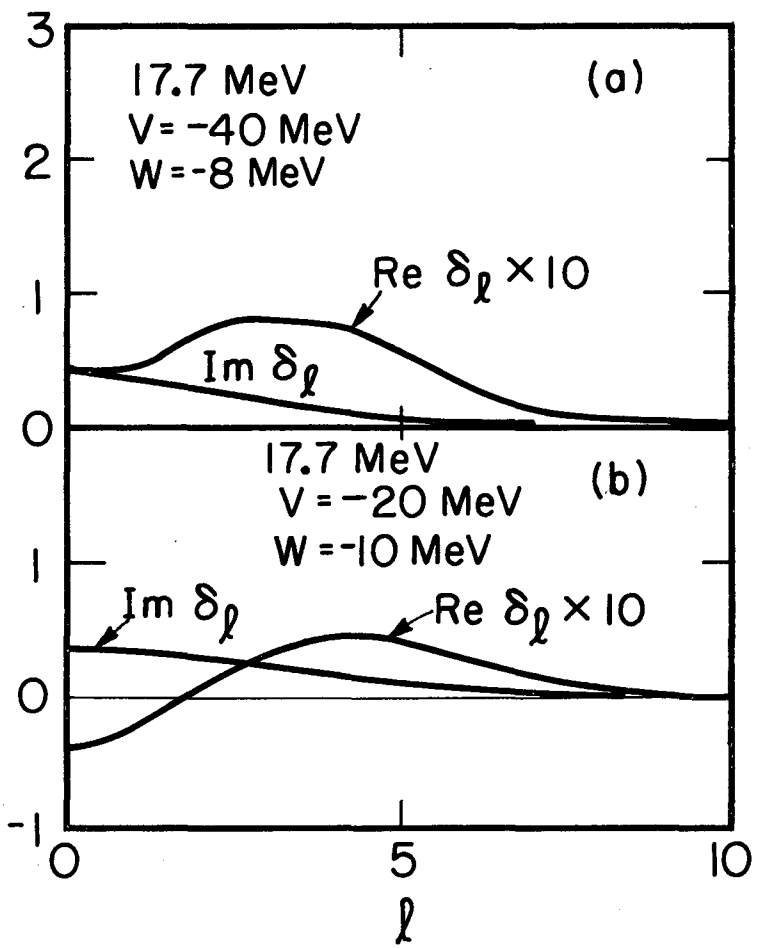

MU-35039

Fig. 6. Real and imaginary parts of the phase shift as functions of the angular momentum. In (b) the magnitude of the absorptive part of the optical potential was increased to 10 MeV; as a result, Reδ_ℓ decreased and became negative for small ℓ.

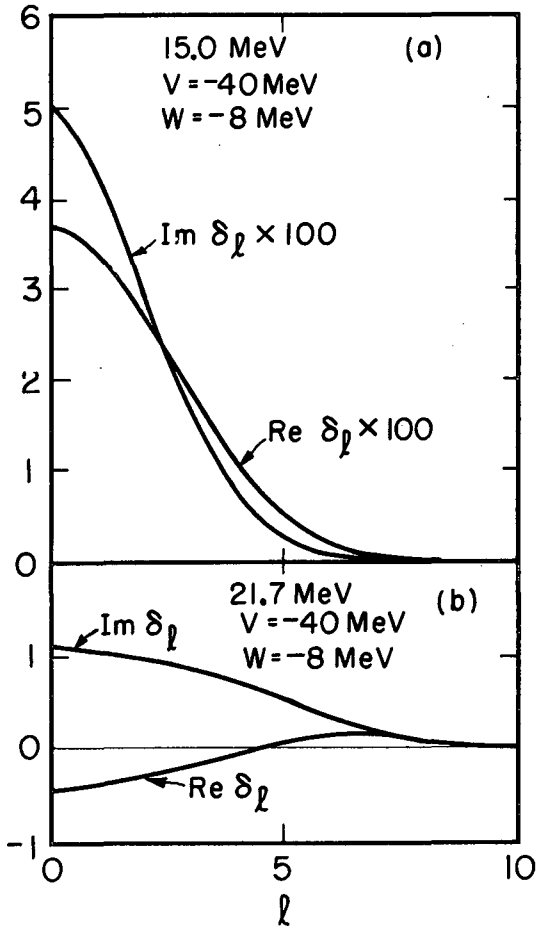

MU-35037

Fig. 7. Real and imaginary parts of the phase shift as functions of the angular momentum. In (b) the incident energy was increased to 21.7 MeV; as a result, Reδ_ℓ became negative for small angular momenta.

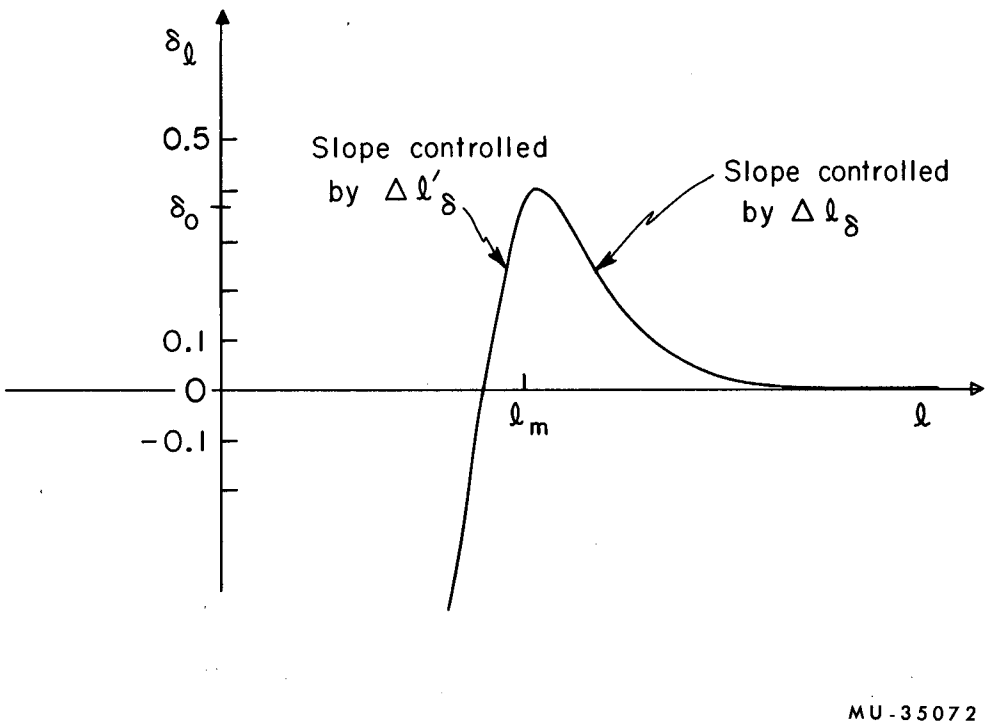

Fig. 8. Nuclear phase shift δ_ℓ as a function of ℓ, according to the present model.

F. Data Analysis

The computational analysis of the data was done on an IBM 7094 electronic computer.

1. Search for Best-Fit Parameters

The experimental values of the ratio $Y^{exp} = (\sigma/\sigma_R)_{exp}$ were fed into a "least-squares" search routine[17] along with the first estimates of the five parameters ℓ_m, $\Delta\ell_A$, δ_0, $\Delta\ell_\delta$, $\Delta\ell'_\delta$. The program, named PHAST VI (for phase-shift analysis), evaluates the function $Y^{calc} = (\sigma/\sigma_R)_{calc}$ and obtains the residuals $DY = (Y^{exp} - Y^{calc})$ at each point (= input c.m. angle). The $\chi^2 = \sum_{i=1}^{N} W_i (DY_i)^2$, where W_i is the weight at each point, is minimized by solving a system of normal equations formed by taking the partial derivatives with respect to each of the parameters. This procedure yields increments to be applied to the original estimates of the parameters. When the parameters appear in a nonlinear fashion in Y_i, as they do in the present case, then the function is first expanded by means of a Taylor series. Repeated iterations are performed which lead to increasingly smaller correction increments to be applied to the previous set of values of the parameters. Normally, the iterative process stops when some convergence criterion is satisfied. In the present case, convergence was achieved when the magnitude of the correction increments became smaller than 10^{-6}. This limit was chosen in order to take into account cases where one or more of the parameters might have been of the order of 10^{-4} or 10^{-5}. In such a case, an increment of the order of 10^{-6} could have been quite important. In the present work none of the five parameters was ever so small. Consequently, the convergence criterion, 10^{-6}, seems to be quite strict, a posteriori. However, it proved to be useful in the present work. In several instances when the correction increment became of the order of 10^{-3} for all parameters, the value of χ^2 kept oscillating strongly from one iteration step to the next. This was a clear indication that for one or more of the parameters the computer was searching in a range of values that produced a narrow local χ^2 minimum. At the end of the iterative process the program calculates and prints the following

relevant quantities: (a) the value of χ^2; (b) the set of values of the five parameters for the best fit; (c) the uncertainty in the parameters; (d) a set of five pairs of "normal" equations, which give the values of the functions

$$EF(K) = \sum_{i=1}^{N} W_i Y_i^{calc} \frac{\partial Y_i}{\partial P_K}$$

and

$$EI(K) = \sum_{i=1}^{N} W_i Y_i^{exp} \frac{\partial Y_i}{\partial P_K} ,$$

where N is the number of input points, K = 1, 2, 3, 4, 5, P_K indicates the relevant parameters, W_i are the weights, and EF(K) and EI(K) should agree to at least six places for a good fit; (e) the calculated function $Y_i^{calc} = (\sigma/\sigma_R)_{calc}$ at each point; (f) the residual $DY_i = (Y_i^{calc} - Y_i^{exp})$ at each point; (g) a 5-by-5 matrix of correlation between the five parameters. The elements of the correlation matrix, a_{KL}, indicate the correlation between parameter K and parameter L:

$$a_{KL} = A^{-1}(K, L)/[A^{-1}(K, K)\ A^{-1}(L, L)]^{-1/2} , \tag{20}$$

where

$$A(K, L) = \sum_i W_i \frac{\partial Y_i}{\partial P_K} \frac{\partial Y_i}{\partial P_L} ,$$

$A^{-1}(K, L)$ is proportional to the covariance between P_K and P_L, and $A^{-1}(K, K)$ and $A^{-1}(L, L)$ are proportional to the variances of P_K and P_L, respectively.[17] Consequently, Eq. (20) is the coefficient of correlation between P_K and P_L.[18]

2. Investigation of the Sensitivity of σ/σ_R to the Parameters

A second program, SENSE, investigates the sensitivity of σ/σ_R to each of the five parameters. We construct a sensitivity function

$$S_{P_K} = \frac{Y^{calc}(P_K) - Y^{calc}(XP_K)}{Y^{calc}(P_K)} , \tag{21}$$

where $Y^{calc}(P_K)$ is the σ/σ_R calculated by using the best-fit parameters, and XP_K is an increment in the parameter P_K; usually X is approximately 0.1 corresponding to a 10% change.

III. EXPERIMENTAL PROCEDURE

A. Objective

The main objective of the heavy-ion experiment was to produce elastic-scattering data accurate to about 1%. Inelastic events associated with excited states of 1 MeV or more could be resolved in the energy spectra of the scattered ion. However, in cases where the target nuclei had low-lying states of excitations of less than 1 MeV, which could be Coulomb-excited, it was necessary to determine the inelastic contamination by another method. To this purpose, a coincidence experiment was performed, between scattered O^{16} ions and the de-excitation γ-rays from Ta^{181}.[19] A second purpose of the coincidence experiment was to compare the experimental determination of the inelastic contribution with that calculated from Coulomb excitation theory,[20] at scattering angles where the theory is applicable; these are the forward angles that accept scattered ions with (classical) impact parameters larger than the nuclear radius.

The objectives of the elastic- and inelastic-scattering experiments were fulfilled. As a result of the Coulomb-excitation measurements, it appears that the theoretically calculated Coulomb-excitation correction can be used at scattering angles where the theory is applicable, thus eliminating the necessity of performing inelastic-scattering experiments in every case where the target nucleus has low-lying states.

B. Apparatus

1. Linear Accelerator

The heavy-ion scattering experiments were performed with the linear accelerator (Hilac) of the Lawrence Radiation Laboratory. The Hilac consists essentially of three parts;[21] a Cockcroft-Walton injector and two 70-Mc cavity resonators of the Alvarez design. A 2-msec pulse of ions from the source with $e/m \geqslant 0.15$ is injected, 10 to 15 times per second, into the first cavity which is called the "prestripper" and contains 37 grid-focussed drift tubes. In the prestripper, the ions are accelerated from 0.07 to 1.0 MeV/nucleon. Before entering the second cavity, called the "poststripper," the ions pass through a film

of matter (stripper) sufficiently thin to avoid multiple scattering and loss of intensity. This increases their e/m ratio to about 0.3, making them subject to greater acceleration. The stripper is a jet of mercury vapor. The poststripper contains 67 drift tubes, each containing a focusing magnet. The rf power used in the two cavities is about 3 MW. Table I shows the ion charge and the beam current, at the three parts of the accelerator, for C^{12} and O^{16} ions.

Table I. Ion charge and beam current at the three parts of the Hilac.

	Injector		Prestripper		Poststripper	
	Charge	Current (μa)	Charge	Current (μa)	Charge	Current (μa)
C^{12}	+2	1400	+2	90	+5	80
O^{16}	+3	800	+3	60	+6	70

The one principal advantage of the linear accelerator is that the stripping process is done at definite stages during the acceleration of the ions, thus eliminating any significant energy spread. The energy of the ions coming out of the machine is 10 MeV/nucleon. There is a possible 0.5 MeV/nucleon energy spread. Figure 9 shows a view of the Hilac.

2. Scattering Chamber and Monitor

The ions were magnetically deflected into the scattering chamber. They entered the chamber through two sets of 1/8-in.-diam collimators. Figure 10 shows the experimental arrangement with the scattering chamber used during the early states. The first set of collimators (1) defined the beam direction. The second set (2) prevented the ions scattered by the walls of the pipe from reaching the target. Two different chambers were used during the course of this experiment. This chamber was 10 in. in diameter and had an 0.002-in. Mylar window on the wall opposite to the beam entrance. The target was placed at the

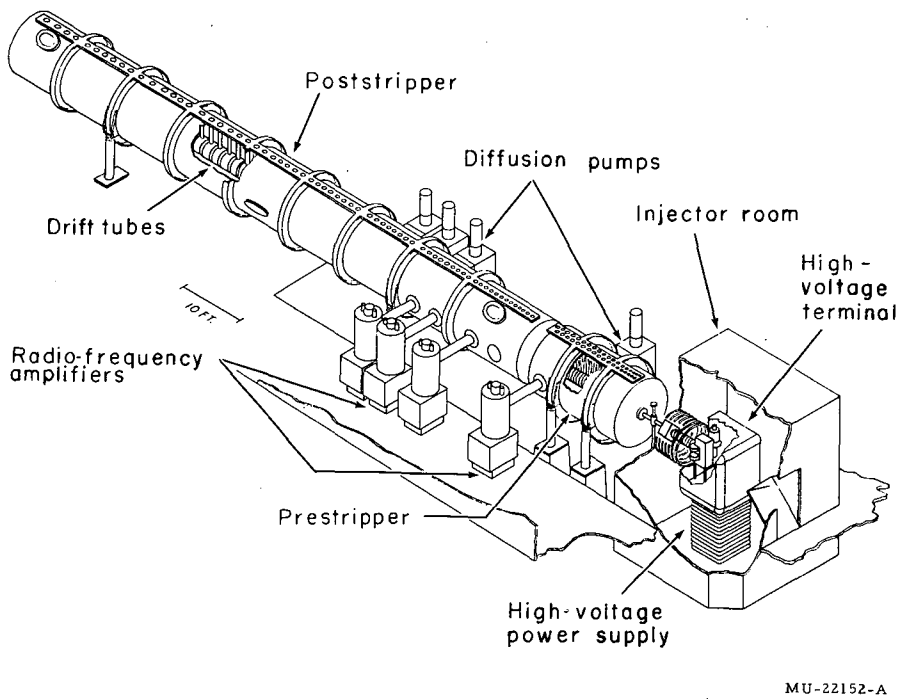

Fig. 9. View of the heavy-ion linear accelerator.

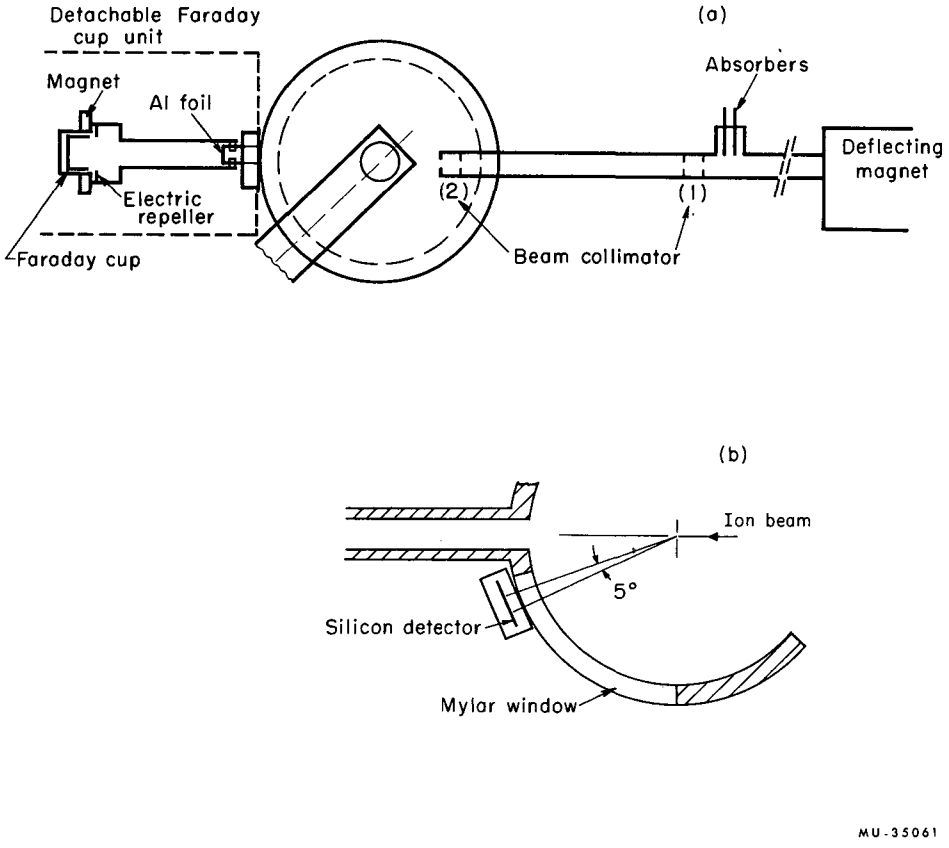

Fig. 10. Scattering chamber used during the early stages of the elastic-scattering experiment.

center of the chamber. The scattered particles, after passing through the Mylar window reached the detector which was mounted on a metal arm that could be rotated around the chamber. A second detecting system, the monitor, was fixed at a permanent position (14 deg). In addition a detachable Faraday cup was utilized to stop the beam outside the far end of the chamber.

The chamber used during the later part of the experiment was a parallelepiped. To avoid multiple scattering due to the Mylar window, the detecting system was placed inside the chamber. It was mounted on a rotating arm and could be moved manually from outside. The monitor system was attached to the lid of the chamber at an angle of 15 deg to the beam. In order to control the monitor counting rate independently over large changes in beam intensity, a disc with collimating holes of various diameters punched along its periphery was placed in front of the monitor. The disc could be rotated manually from the outside. As the beam intensity increased, collimating holes of smaller and smaller diameter were placed in front of the monitor so that the beam flux through the detector was kept safely low. Figure 11 shows the experimental arrangement with the second scattering chamber. For the coincidence experiment a third (NaI) detector was placed underneath the scattering chamber as shown in Fig. 12.

3. Detectors and Electronic Equipment

Solid-state silicon detectors were used throughout this experiment for the detection of the scattered ions. The detectors were furnished with a guard ring that effectively reduced the surface leakage current which frequently interferes with the accurate performance of p-n junction detectors.[22] The linear response of the detectors to the energy lost by the incident particles independent of their charge, mass, or velocity results in a very high energy resolution. In order to increase the depletion layer of the detector, which is the effective thickness where the particle detection takes place, a reverse bias voltage was applied. Theoretically the effective thickness is given by

$$W = 1.05 \frac{[\epsilon(V_0 + V_b)]^{1/2}}{2\pi e N} \times 10^{-6} \text{ cm} . \qquad (22)$$

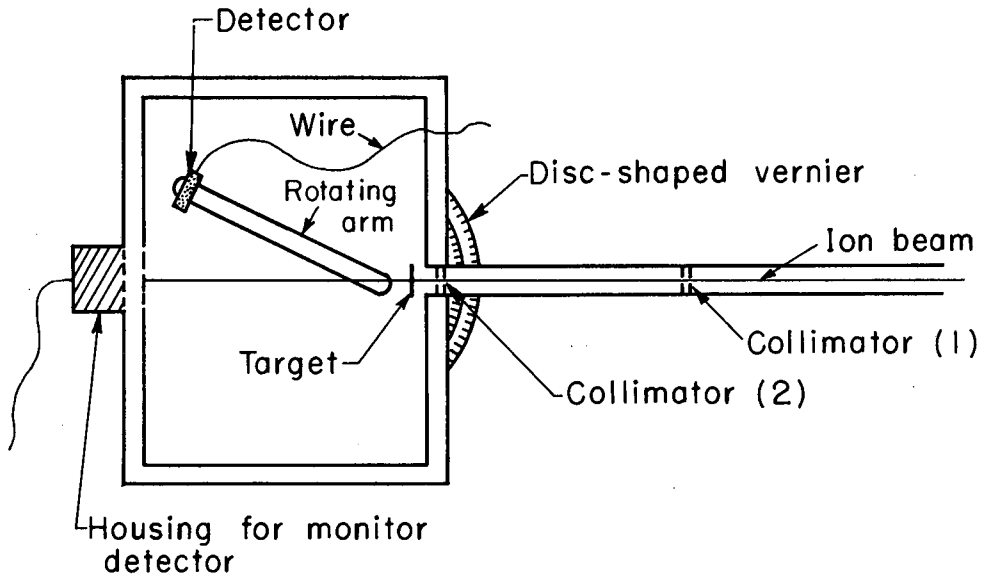

MU-35060

Fig. 11. Scattering chamber used during the later stage of the elastic-scattering experiment. The monitor detector is at an angle of 15 deg with the beam level.

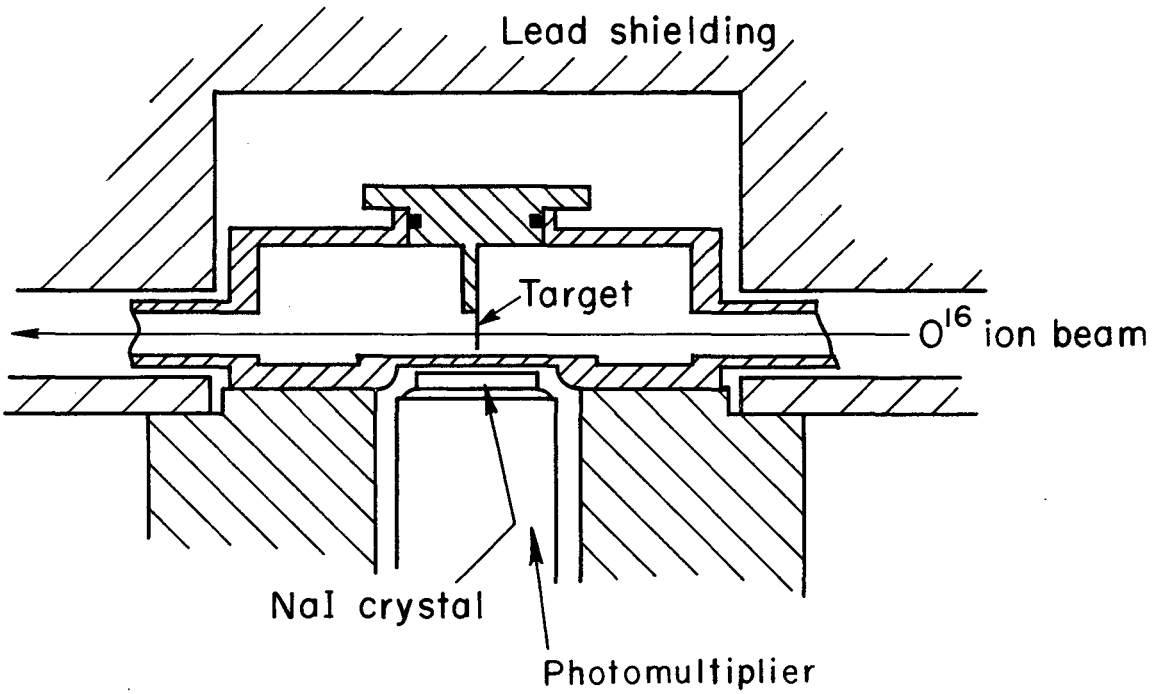

MU-35059

Fig. 12. Experimental arrangement for the inelastic-scattering experiment.

Here, ϵ is the dielectric constant of silicon, e is the electronic charge, V_0 is the potential created at the junction when no external voltage is applied, and V_b is the reverse bias voltage (positive on the N side). Figure 13 shows the experimental arrangement of a guard-ring detector. In the elastic-scattering experiment, the pulses from the detector were fed in turn into a preamplifier, a linear amplifier, and a 100-channel pulse-height analyzer (Penco). They were also recorded in a scaler. In the inelastic-scattering experiment the electronic system was far more complicated, as Fig. 14 shows.

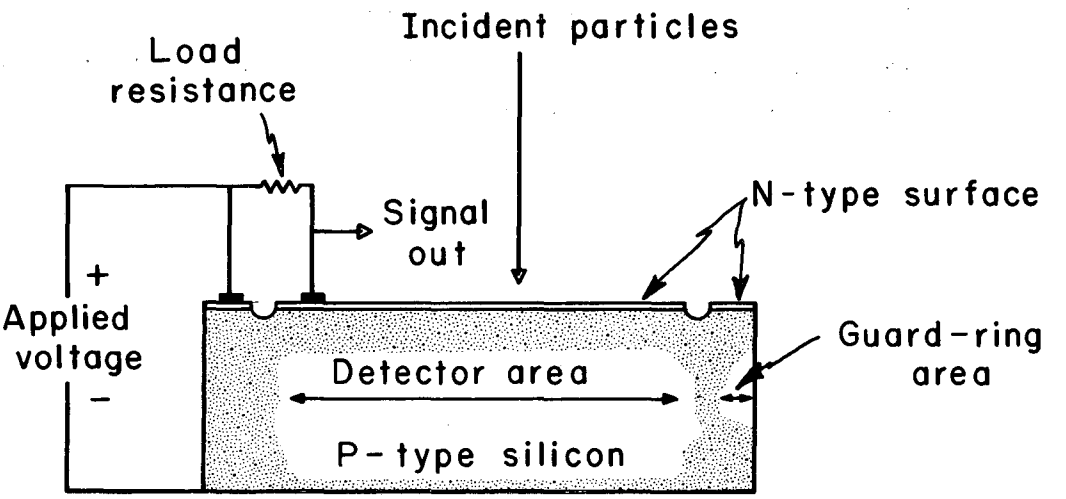

MU-35065

Fig. 13. Guard ring solid-state silicon detector.

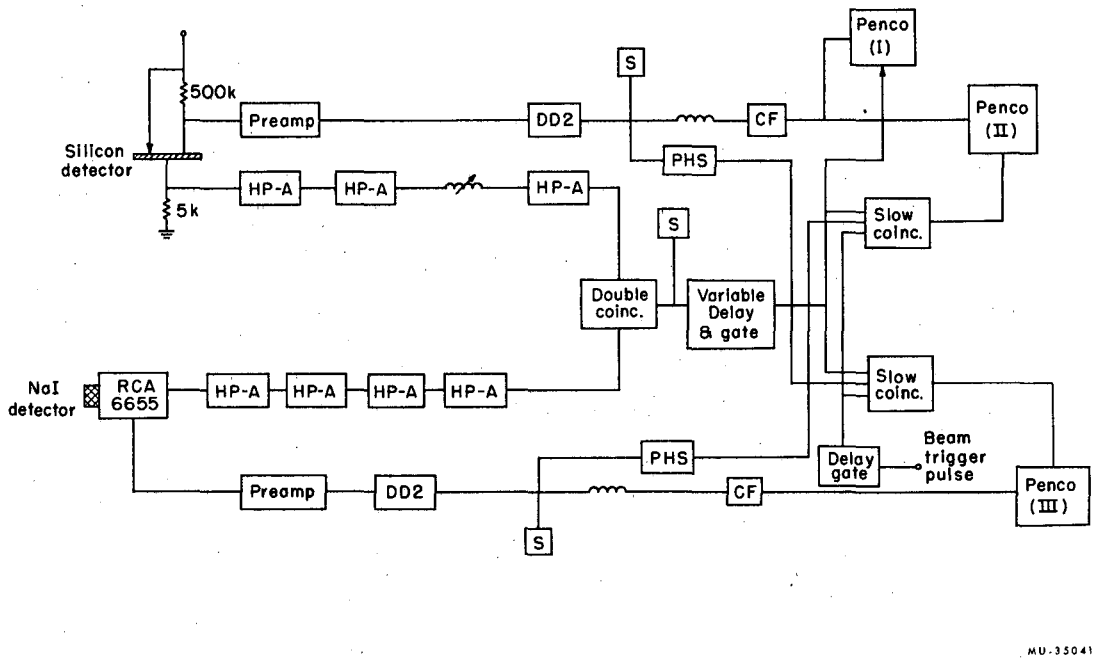

Fig. 14. Block diagram of the electronics for the inelastic-scattering experiment.

IV. EXPERIMENTAL RESULTS AND THEORETICAL ANALYSIS

A. Elastic Scattering

Tables II to XXXIII contain experimental data[23-29] and the results of the theoretical analysis of the data, for sixteen different projectile-target systems at various laboratory energies. Figures 15 to 30 present the experimental values for σ/σ_R as a function of the scattering angle, and the theoretical curve obtained by means of Eqs. (14), (17), and (19) and the best-fit parameters that appear in the respective tables. The interaction radius R was calculated from Eq. (10), and the nuclear surface thickness, ΔR, from Eq. (16). The $A^{1/3}$ law was then used in the form

$$R = R_n + R_{projectile} = r_a A^{1/3} + R_{projectile} \tag{23}$$

to obtain the radius parameter r_a.

Table XXXIV presents a summary of the results for r_a and ΔR and Fig. 31 shows a plot of the nuclear radius, R_n vs $A^{1/3}$.

For heavy-ion scattering, R_p was also set equal to $r_a A_p^{1/3}$. This yielded the radii of C^{12} and O^{16}. Bearing in mind the negligible difference in the radii of the Pb isotopes,[30] we compared the O^{16} - Pb^{208} and C^{12} - Pb^{208} systems to the α - $Pb^{(nat.)}$. This yielded an α-particle radius

$$R_\alpha = 2.192 \times 10^{-13} \text{ cm} .$$

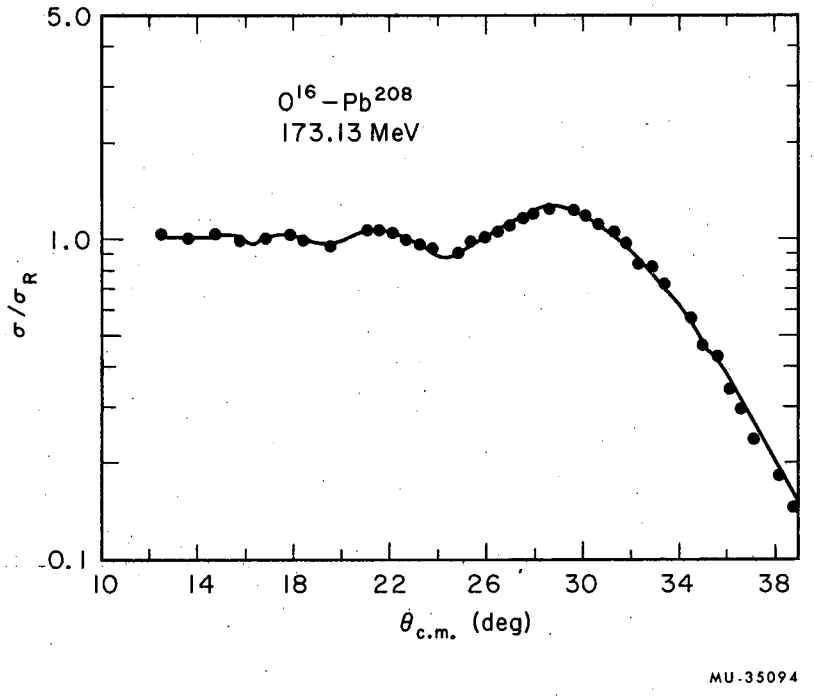

Fig. 15. Angular distribution of O^{16} ions elastically scattered from Pb^{208} at $E_{lab} = 173.36$ MeV. The dots represent the experimental cross section, and the solid line is the calculated cross section with the values of the parameters as they appear in Table III.

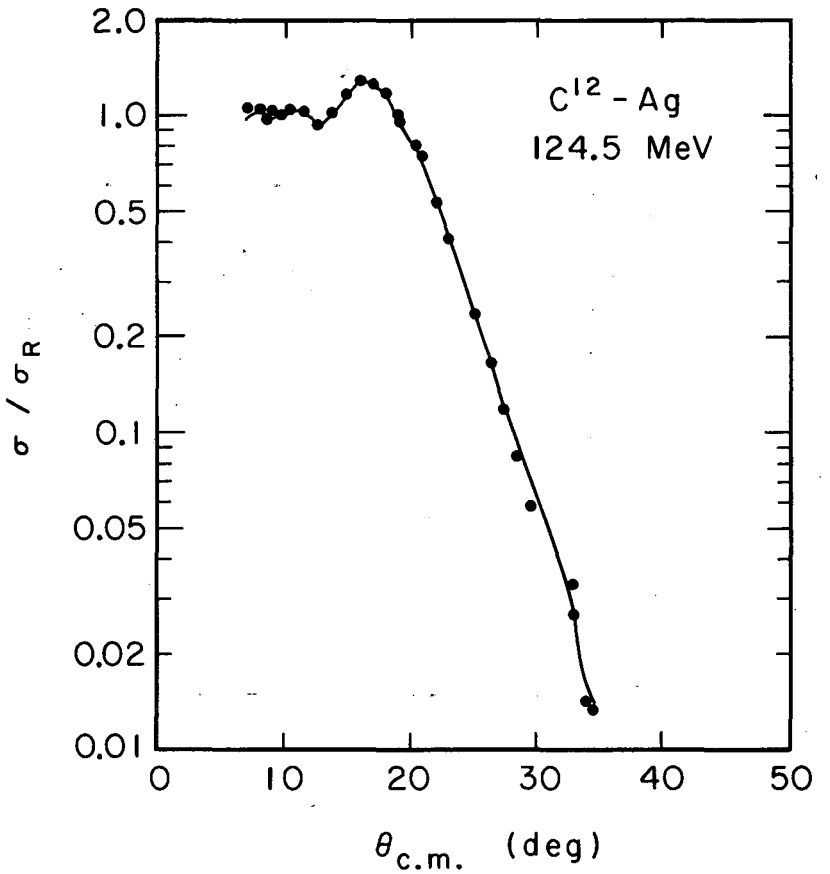

MU-35067

Fig. 18. Angular distribution of C^{12} ions elastically scattered from Ag at $E_{lab} = 124.5$ MeV. The dots represent the experimental cross section, and the solid line is the calculated cross section with the values of the parameters as they appear in Table IX.

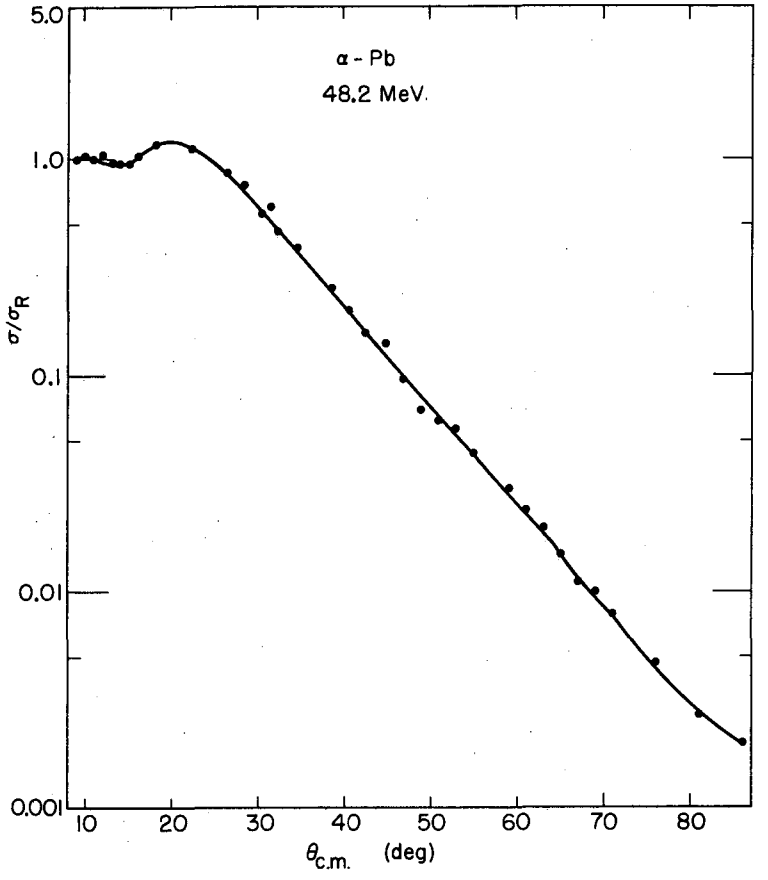

Fig. 19. Angular distribution of α particles elastically scattered from Pb at $E_{lab} = 48.2$ MeV. The dots represent the experimental cross section, and the solid line is the calculated cross section with the values of the parameters as they appear in Table XI.

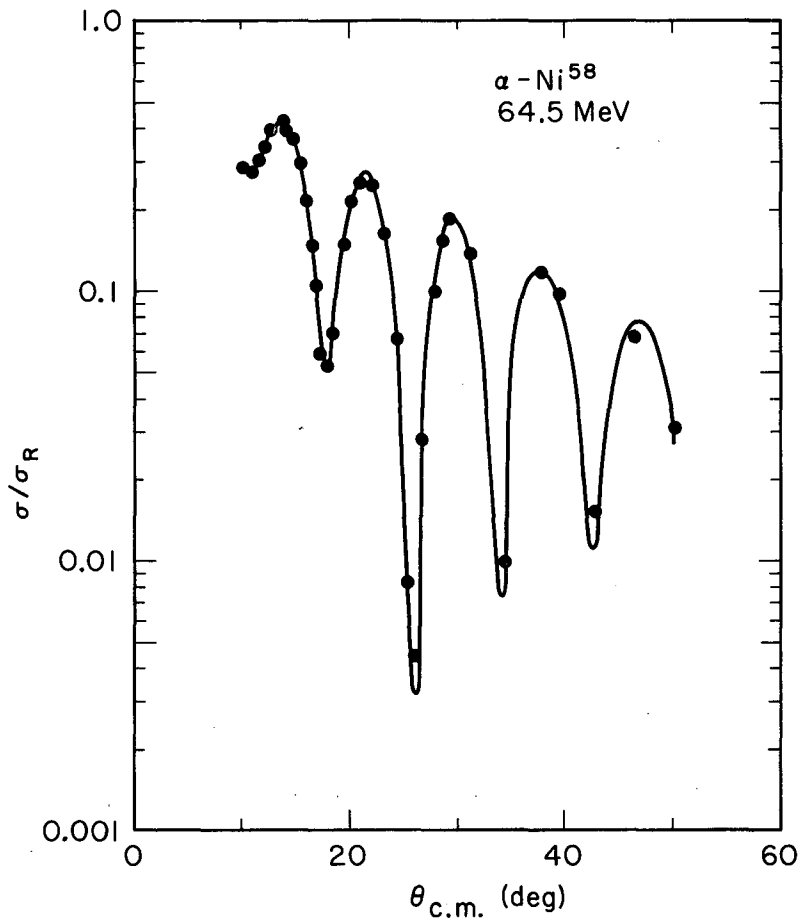

MU-35011

Fig. 20. Angular distribution of α particles elastically scattered from Ni^{58} at $E_{lab} = 64.3$ MeV. The dots represent the experimental cross section, and the solid line is the calculated cross section with the values of the parameters as they appear in Table XIII.

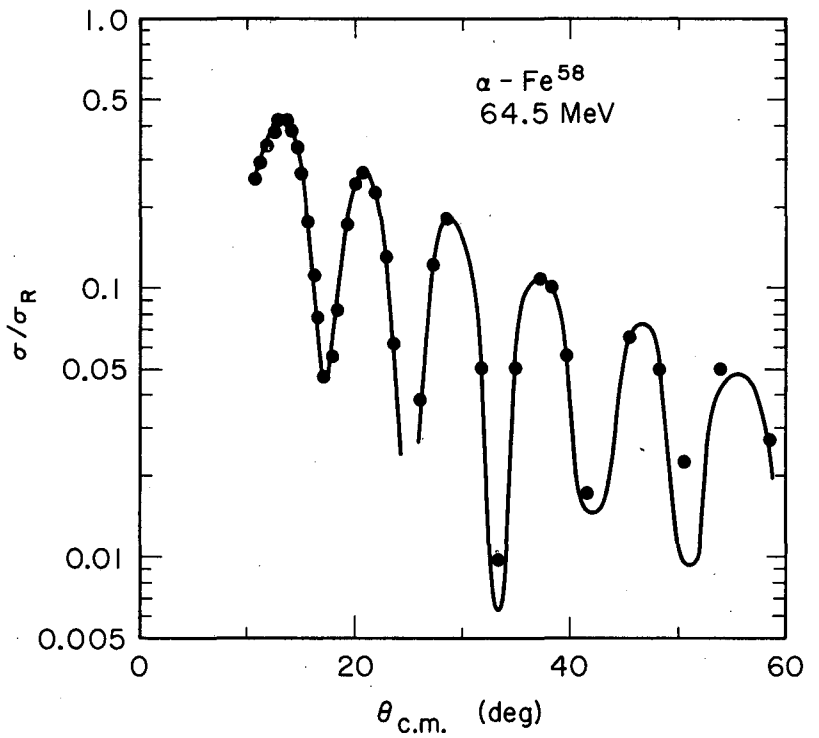

MU-35015

Fig. 21. Angular distribution of α particles elastically scattered from Fe^{58} at $E_{lab} = 64.3$ MeV. The dots represent the experimental cross section, and the solid line is the calculated cross section with the values of the parameters as they appear in Table XV.

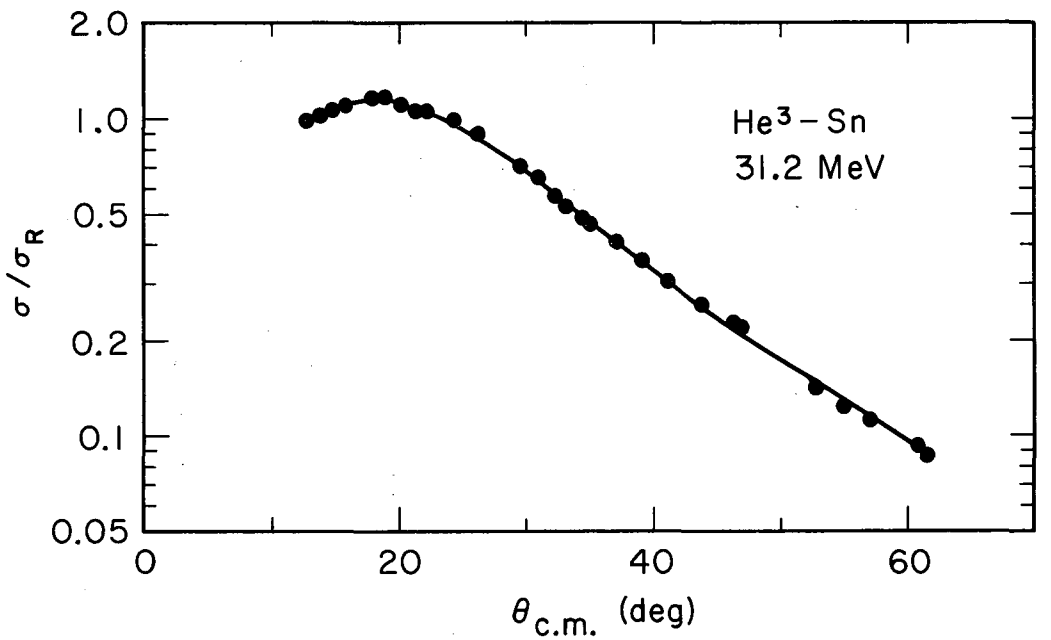

MU-35017

Fig. 22. Angular distribution of He^3 ions elastically scattered from Sn at $E_{lab} = 31.2$ MeV. The dots represent the experimental cross section, and the solid line is the calculated cross section with the values of the parameters as they appear in Table XVII.

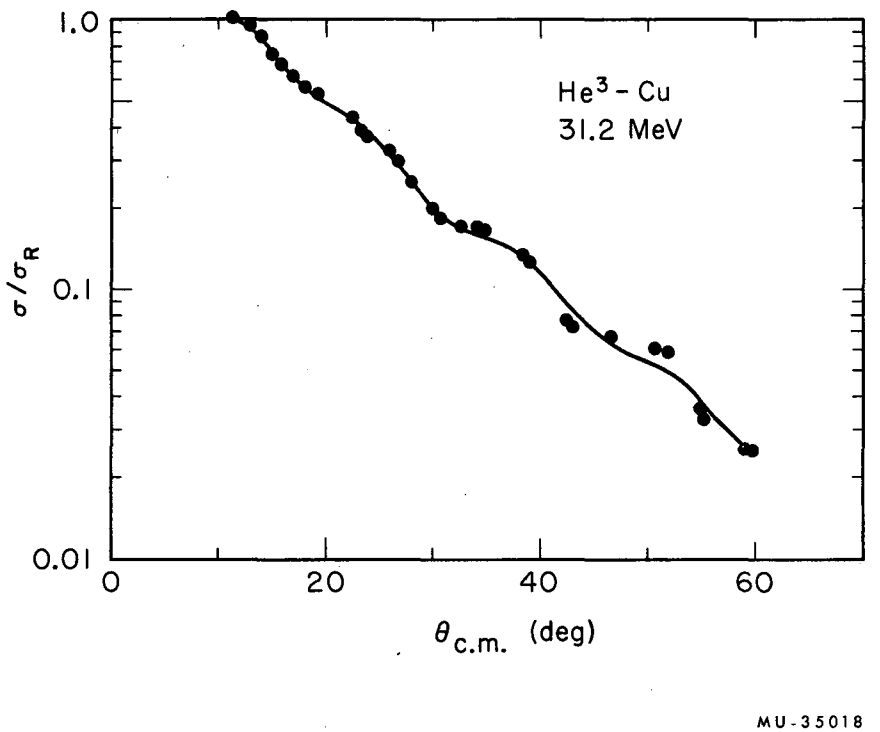

Fig. 23. Angular distribution of He^3 ions elastically scattered from Cu at $E_{lab} = 31.2$ MeV. The dots represent the experimental cross section, and the solid line is the calculated cross section with the values of the parameters as they appear in Table XIX.

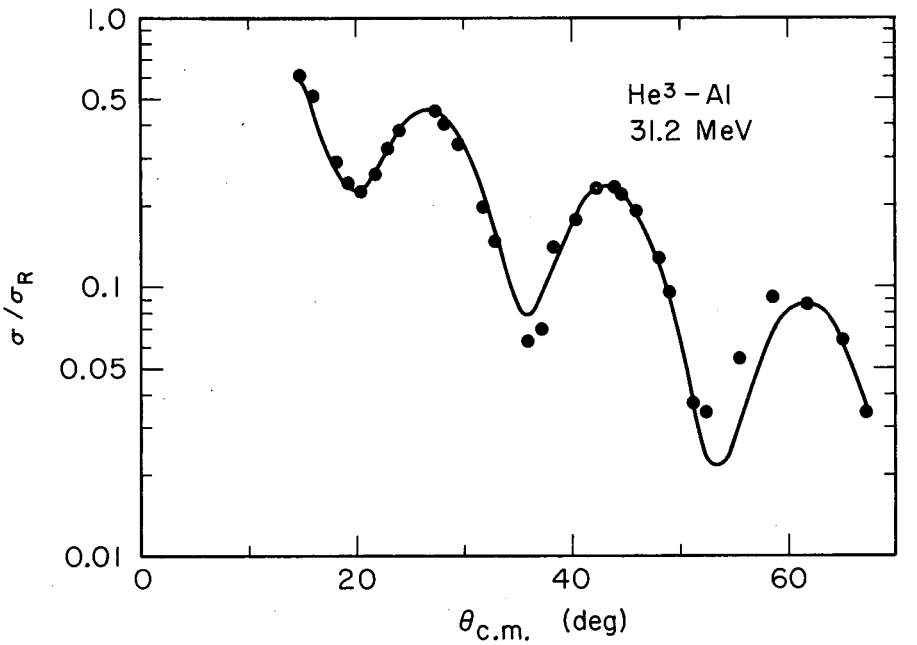

MU-35019

Fig. 24. Angular distribution of He^3 ions elastically scattered from Al at $E_{lab} = 31.2$ MeV. The dots represent the experimental cross section, and the solid line is the calculated cross section with the values of the parameters as they appear in Table XXI.

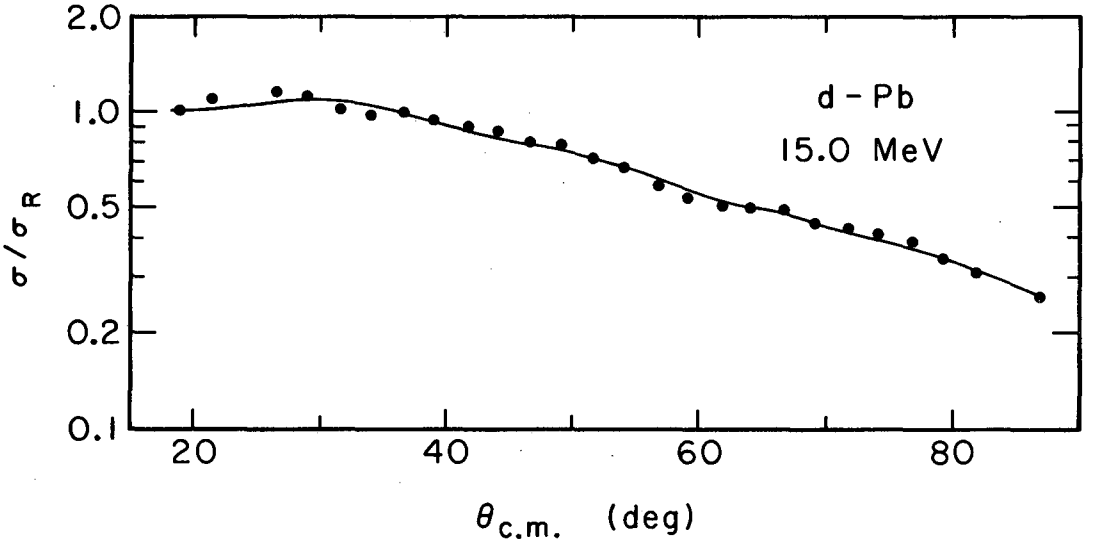

MU-35070

Fig. 25. Angular distribution of deuterons elastically scattered from Pb at $E_{lab} = 15.0$ MeV. The dots represent the experimental cross section, and the solid line is the calculated cross section with the values of the parameters as they appear in Table XXIII.

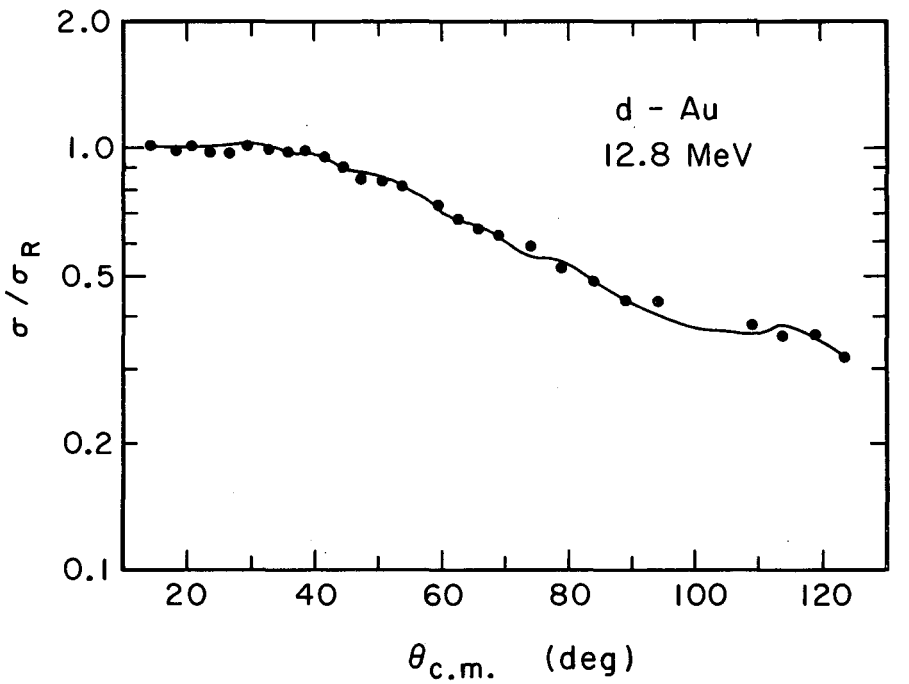

MU-35066

Fig. 26. Angular distribution of deuterons elastically scattered from Au at $E_{lab} = 12.8$ MeV. The dots represent the experimental cross section, and the solid line is the calculated cross section with the values of the parameters as they appear in Table XXV.

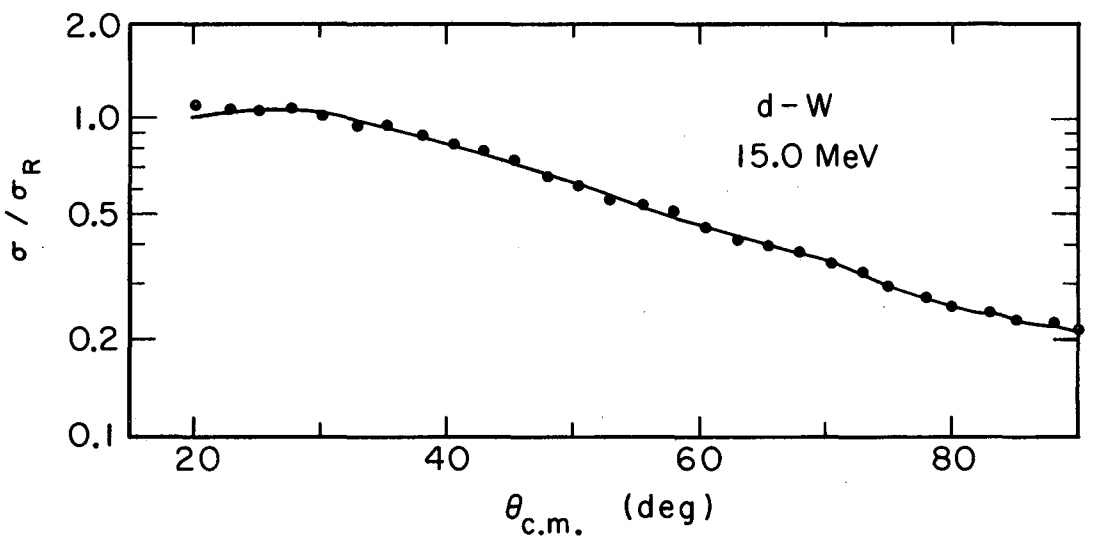

MU-35068

Fig. 27. Angular distribution of deuterons elastically scattered from W at $E_{lab} = 15.0$ MeV. The dots represent the experimental cross section, and the solid line is the calculated cross section with the values of the parameters as they appear in Table XXVII.

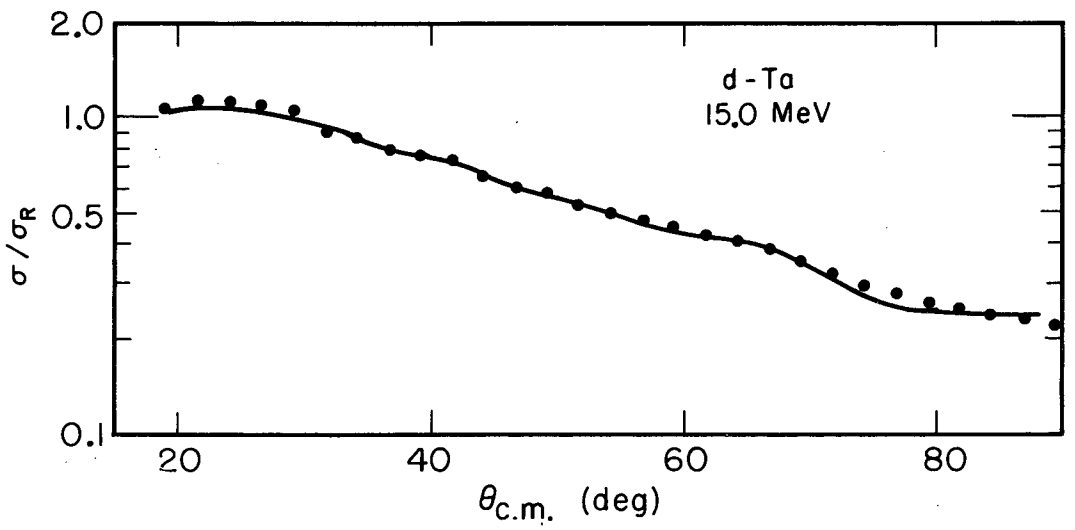

MU-35038

Fig. 28. Angular distribution of deuterons elastically scattered from Ta at $E_{lab} = 15.0$ MeV. The dots represent the experimental cross section, and the solid line is the calculated cross section with the values of the parameters as they appear in Table XXIX.

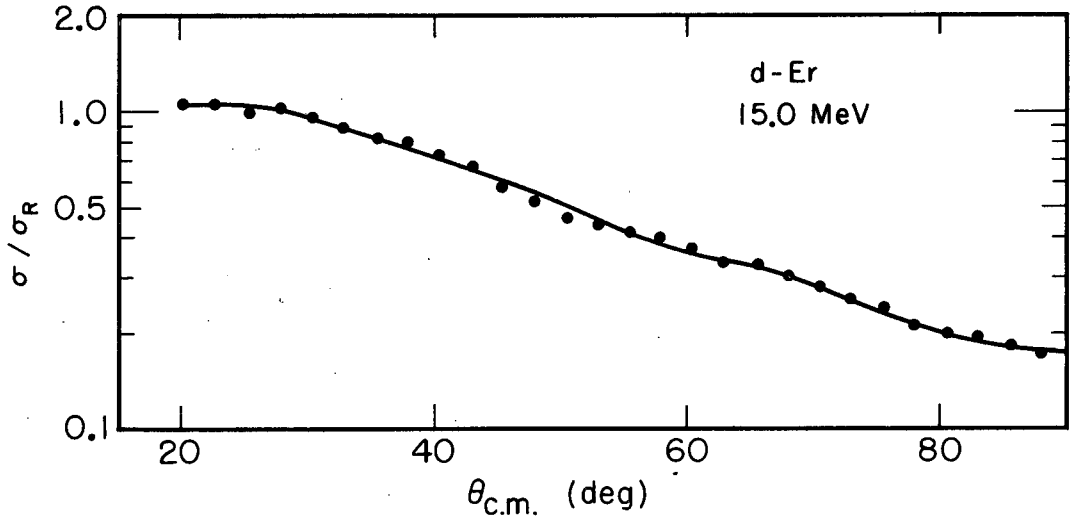

MU-35040

Fig. 29. Angular distribution of deuterons elastically scattered from Er at $E_{lab} = 15.0$ MeV. The dots represent the experimental cross section, and the solid line is the calculated cross section with the values of the parameters as they appear in Table XXXI.

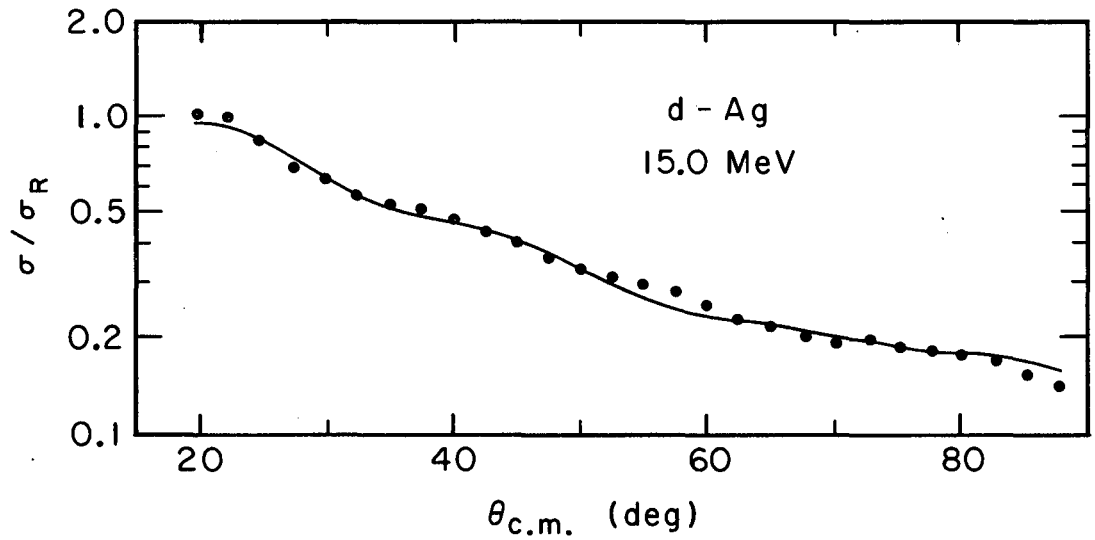

MU-35069

Fig. 30. Angular distribution of deuterons elastically scattered from Ag at $E_{lab} = 15.0$ MeV. The dots represent the experimental cross section, and the solid line is the calculated cross section with the values of the parameters as they appear in Table XXXIII.

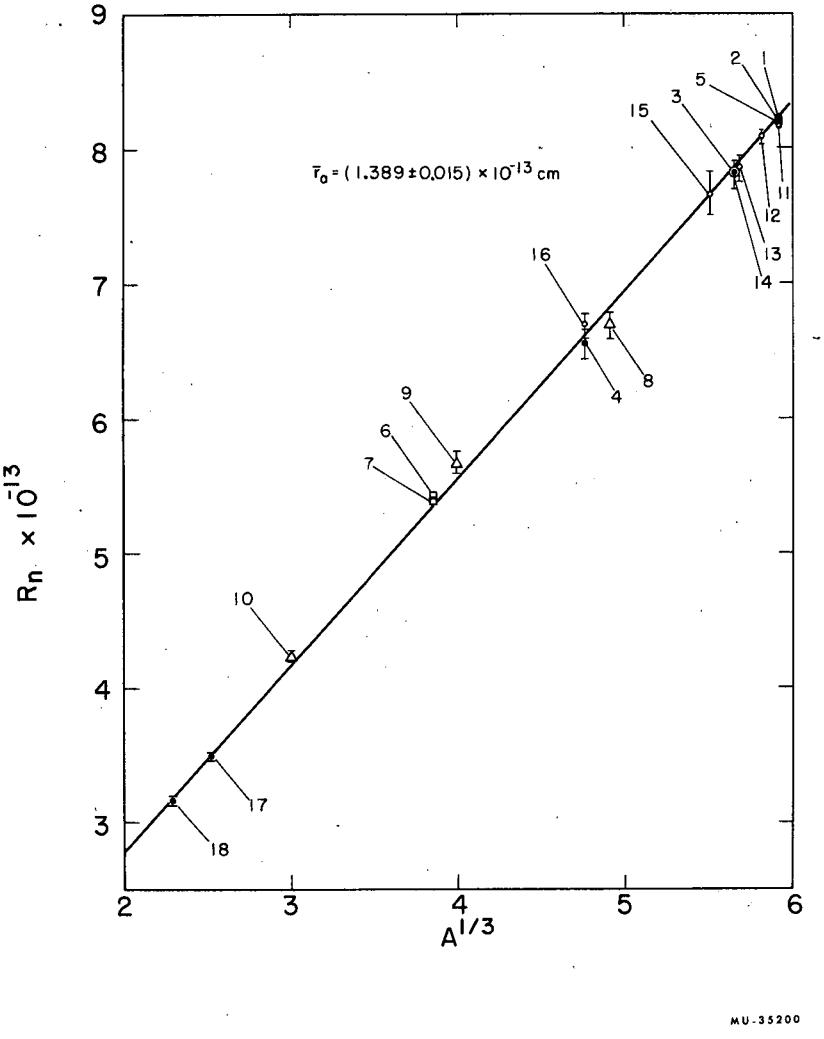

Fig. 31. Nuclear radius R_n vs $a^{1/3}$.

Table II. Experimental results:[23]
O^{16} - Pb^{208}; E_{lab} = 173.36 MeV.

$\theta_{c.m.}$ (deg)	σ/σ_R	Error (%)	$\theta_{c.m.}$ (deg)	σ/σ_R	Error (%)
12.52	1.032	4.0	28.09	1.177	1.8
13.60	1.013	3.3	28.63	1.238	1.9
14.68	1.029	3.6	27.70	1.229	1.8
15.75	0.979	3.7	30.23	1.169	1.8
16.83	0.945	3.2	30.76	1.119	2.1
17.90	1.036	2.9	31.30	1.058	2.2
18.44	0.992	3.2	31.84	0.960	2.2
19.51	0.948	3.2			
20.05	1.008	3.0	32.89	0.814	2.3
21.13	1.062	3.0	33.43	0.719	3.2
21.67	1.059	3.4	33.96	0.623	4.0
22.20	6.042	2.8	34.50	0.569	4.3
22.74	0.989	3.4	35.03	0.460	4.3
23.28	0.947	3.2	35.57	0.422	5.0
23.81	0.932	2.1	36.10	0.337	7.6
24.88	0.904	2.6	36.63	0.294	5.6
25.42	0.979	2.0	37.16	0.236	7.5
25.95	1.012	1.9	38.23	0.1803	5.8
26.49	1.058	1.8	38.75	0.1443	9.6
27.02	1.116	1.8	39.28	0.1258	10.5
27.56	1.167	1.8			

$Z = 79$, $E_{c.m.} = 158.0$ MeV, $\lambda\!\!\!^{-} = 0.094$f, $n = 31.66$, $v = 4.53 \times 10^9$ cm/sec.

Table III. Theoretical analysis: O^{16} - Pb^{208}, E_{lab} = 173.36 MeV.

Best-fit parameters	ℓ_m = 86.462 ± 0.73	$\Delta\ell_A$ = 7.305 ± 0.48	δ = 1.495 ± 0.05	$\Delta\ell_\delta$ = 6.46 ± 0.69	$\Delta\ell'_\delta$ = 18.805 ± 1.52
Transition region in ℓ-space	$\Delta\ell = (4.4)\Delta\ell_A = 32.14 \pm 2.11$				
Radius of interaction	$R = 11.722 \times 10^{-13}$ cm				
Absorption parameter	$r_a = (1.388 \pm 0.008) \times 10^{-13}$ cm				
Nuclear radius	$R_n = r_a A^{1/3} = (8.22 \pm 0.05) \times 10^{-13}$ cm				
Nuclear-surface thickness	$\Delta R = (2.85 \pm 0.2) \times 10^{-13}$ cm				
Total reaction cross section σ_R = 2.520 b.					

Table IV. Experimental results:[23]
C^{12} - Pb^{208}; E_{lab} = 127.55 MeV.

$\theta_{c.m.}$ (deg)	σ/σ_R	$\theta_{c.m.}$ (deg)	σ/σ_R
14.88	0.976	30.46	1.15
15.95	1.073	31.10	1.109
18.07	0.947	31.51	1.024
19.13	1.01	31.84	0.994
20.19	1.025	32.16	0.928
21.25	1.034	32.58	0.914
21.69	0.986	32.89	0.837
22.30	0.962	33.21	0.801
23.05	0.937	33.63	0.735
23.68	0.942	33.95	0.667
24.10	0.980	34.27	0.641
24.75	1.017	34.69	0.596
25.49	1.071	35.0	0.556
25.80	1.12	35.32	0.537
26.55	1.196	35.74	0.494
27.29	1.287	36.06	0.429
28.35	1.325	36.38	0.417
29.40	1.222	37.10	0.326
		37.42	0.301
		37.84	0.296

$Z = 82$, $E_{c.m.} = 118.4$ MeV, $\lambda\!\!\!^{-} = 0.124$f, $n = 23.98$, $v = 4.49 \times 10^9$ cm/sec.

Table V. Theoretical analysis: C^{12} - Pb^{208}, E_{lab} = 127.55 MeV.

Best-fit parameters	$\ell_m = 62.22 \pm 0.7$	$\Delta\ell_A = 4.597 \pm 0.53$	$\delta = 1.56 \pm 0.09$	$\Delta\ell_\delta = 6.737 \pm 0.5$	$\Delta\ell'_\delta = 15.3 \pm 2.2$
Transition region in ℓ-space	$\Delta\ell = (4.4)\Delta\ell_A = 20.21 \pm 2.33$				
Radius of interaction	$R = (11.36 \pm 0.15) \times 10^{-13}$ cm				
Absorption parameter	$r_a = (1.383 \pm 0.01) \times 10^{-13}$ cm				
Nuclear radius	$R_n = r_a A^{1/3} = (8.197 \pm 0.06) \times 10^{-13}$ cm				
Nuclear-surface thickness	$\Delta R = (2.35 \pm 0.27) \times 10^{-13}$ cm				

Total reaction cross section: $\sigma_R = 2.24$ b.

Table VI. Experimental results:[24]
C^{12} - Ta; E_{lab} = 124.5 MeV.

$\theta_{c.m.}$ (deg)	σ/σ_R	$\theta_{c.m.}$ (deg)	σ/σ_R
7.9	0.99	25.3	1.29
9.0	1.01	26.4	1.25
10.1	1.01	27.4	1.22
11.1	0.98	28.5	1.09
12.1	0.96	29.5	0.94
13.2	0.97	30.6	0.81
14.3	1.01	31.6	0.67
15.4	0.98	33.3	0.46
16.4	0.99	34.3	0.38
17.5	1.04	34.9	0.312
18.6	1.05	35.8	0.25
19.6	0.98	37.6	0.166
20.9	0.91	38.7	0.122
22.1	0.96	39.6	0.103
23.2	1.09	41.2	0.063
24.2	1.19		

$Z = 73$, $E_{c.m.} = 114.6$ MeV, $\lambda\!\!\!^{-} = 0.1272$f, $n = 21.61$, $v = 4.433 \times 10^9$ cm/sec.

Table VII. Theoretical analysis: C^{12} - Ta^{181}, E_{lab} = 124.5 MeV.

Best-fit parameters	$\ell_m = 60.51 \pm 0.12$	$\Delta\ell_A = 4.779 \pm 0.68$	$\delta = 1.369 \pm 0.04$	$\Delta\ell_\delta = 5.323 \pm 0.7$	$\Delta\ell'_\delta = 7.689 \pm 2.19$
Transition region in ℓ-space	$\Delta\ell = (4.4)\Delta\ell_A = 21.03 \pm 2.99$				
Radius of interaction	$R = (10.98 \pm 0.15) \times 10^{-13}$ cm				
Absorption	$r_a = (1.382 \pm 0.018) \times 10^{-13}$				
Nuclear radius	$R_n = r_a A^{1/3} = (7.818 \pm 0.1) \times 10^{-13}$ cm				
Nuclear-surface thickness	$\Delta R = (2.52 \pm 0.36) \times 10^{-13}$				
Total reaction cross section $\sigma_R = 2.227$ b.					

Table VIII. Experimental results:[24]
C^{12} - Ag; E_{lab} = 124.5 MeV.

$\theta_{c.m.}$ (deg)	σ/σ_R	Error (%)	$\theta_{c.m.}$ (deg)	σ/σ_R	Error (%)
6.9	1.050	1.0	19.2	0.948	1.0
8.0	1.054	1.0	20.3	0.806	1.0
8.6	0.969	1.0	20.7	0.738	1.0
9.1	1.033	1.0	21.6	0.980	1.0
9.7	0.996	1.0	21.9	0.530	1.0
10.4	1.056	1.0	23.0	0.409	1.0
11.5	1.031	1.0	25.0	0.234	2.0
12.6	0.931	1.0	26.3	0.167	1.0
13.7	1.027	1.0	27.4	0.118	1.5
14.8	1.151	1.0	28.5	0.0842	1.5
16.0	1.279	1.0	27.6	0.0584	1.5
17.0	1.248	1.0	32.9	0.0331	2.0
18.2	1.177	1.0	34.0	0.0142	3.0
19.0	1.014	1.0	34.4	0.0133	1.5

$Z = 47$, $E_{c.m.} = 110.0$ MeV, $\lambda = 0.132$f, $n = 13.91$, $v = 4.433 \times 10^9$ cm/sec.

Table IX. Theoretical analysis: C^{12} - Ag, E_{lab} = 124.5 MeV.

Best-fit parameters	$\ell_m = 57.251 \pm 1.23$	$\Delta\ell_A = 3.89 \pm 0.60$	$\delta = 1.51 \pm 0.09$	$\Delta\ell_\delta = 8.60 \pm 1.18$	$\Delta\ell'_\delta = 39.62 \pm 8.87$
Transition region in ℓ-space	$\Delta\ell = (4.4)\Delta\ell_A = 17.12 \pm 2.64$				
Radius of interaction	$R = (9.721 \pm 0.16) \times 10^{-13}$ cm				
Absorption parameter	$r_a = (1.379 \pm 0.023) \times 10^{-13}$ cm				
Nuclear radius	$R_n = r_a A^{1/3} = (6.564 \pm 0.11) \times 10^{-13}$ cm				
Nuclear-surface thickness	$\Delta R = (2.2 \pm 0.36) \times 10^{-13}$ cm				
Total reaction cross section: $\sigma_R = 2.11$ b.					

Table X. Experimental results:[25]

α - Pb; E_{lab} = 48.2 MeV.

$\theta_{c.m.}$ (deg)	σ/σ_R	Error (%)	$\theta_{c.m.}$ (deg)	σ/σ_R	Error (%)
9.17	1.0	1.3	40.71	0.201	1.7
10.19	1.034	1.1	42.74	0.158	1.5
11.21	1.023	1.3	44.77	0.143	1.6
12.23	1.049	1.3	46.79	0.0959	1.4
13.25	0.973	1.2	48.82	0.0699	1.5
14.27	0.963	1.0	50.84	0.0620	1.7
15.29	0.967	1.2	52.87	0.0570	1.7
16.30	1.044	1.3	54.89	0.0440	2.0
18.34	1.153	1.5	58.93	0.0300	1.8
20.38	1.265	1.1	60.95	0.0240	2.1
22.41	1.133	1.0	62.97	0.0197	2.5
26.48	0.866	1.1	64.99	0.0147	2.2
28.52	0.765	1.4	67.01	0.0110	1.8
30.55	0.563	1.3	69.02	0.0101	1.6
31.57	0.603	1.3	71.04	0.00789	2.1
32.58	0.466	1.5	76.06	0.00470	3.4
34.62	0.389	1.2	81.09	0.00273	2.5
38.68	0.254	1.3	86.10	0.00199	3.3

$Z = 82$, $E_{c.m.} = 46.3$ MeV, $\lambda = 0.339$f, $n = 7.52$, $v = 4.77 \times 10^9$ cm/sec.

Table XI. Theoretical analysis: α - Pb, E_{lab} = 48.2 MeV.

Best-fit parameters	$\ell_m = 21.36 \pm 0.29$	$\Delta\ell_A = 1.234 \pm 0.06$	$\delta = 1.19 \pm 0.026$	$\Delta\ell_\delta = 2.238 \pm 0.66$	$\Delta\ell'_\delta = 34.13 \pm 1.17$
Transition region in ℓ-space	$\Delta\ell = (4.4)\Delta\ell_A = 5.43 \pm 0.26$				
Radius of interaction	$R = (10.384 \pm 0.096) \times 10^{-13}$ cm				
Absorption parameter	$r_a = (1.383 \pm 0.013) \times 10^{-13}$ cm				
Nuclear radius	$R_n = r_a A^{1/3} = (8.192 \pm 0.07) \times 10^{-13}$ cm				
Nuclear-surface thickness	$\Delta R = (1.74 \pm 0.10) \times 10^{-13}$ cm				
Total reaction cross section: $\sigma_R = 1.939$ b.					

Table XII. Experimental results:[26]
α - Ni^{58}; E_{lab} = 64.5 MeV.

$\theta_{c.m.}$ (deg)	σ/σ_R	Error (%)	$\theta_{c.m.}$ (deg)	σ/σ_R	Error (%)
10.36	0.28973	0.2	21.11	0.2552	0.2
10.97	0.2766	0.19	22.18	0.2461	0.19
11.61	0.3060	0.2	23.20	0.1649	0.18
12.11	0.3447	0.24	24.36	0.06767	0.06
12.97	0.4025	0.24	25.41	0.008357	0.03
13.23	0.4154	0.25	25.89	0.004407	0.01
13.72	0.4295	0.26	26.68	0.02832	0.05
14.30	0.3963	0.24	27.77	0.1036	0.06
14.82	0.3684	0.29	28.60	0.15804	0.07
15.41	0.3001	0.3	29.29	0.1872	0.28
15.93	0.21898	0.19	31.24	0.14026	0.1
16.49	0.1491	0.15	34.44	0.01018	0.04
16.94	0.1054	0.12	37.86	0.1199	0.1
17.44	0.0594	0.07	39.66	0.10016	0.1
17.96	0.05471	0.08	42.88	0.01535	0.07
18.48	0.07059	0.07	46.38	0.06848	0.08
19.47	0.1481	0.1	50.23	0.03214	0.1
20.33	0.2161	0.4			

$Z = 28$, $E_{c.m.} = 58.54$ MeV, $\lambda = 0.309$, $n = 2.229$, $v = 5.494 \times 10^9$ cm/sec.

Table XIII. Theoretical analysis: α - Ni^{58}, E_{lab} = 64.5 MeV.

Best-fit parameters	$\ell_m = 21.69 \pm 0.43$	$\Delta\ell_A = 1.108 \pm 0.07$	$\delta = 1.401 \pm 0.043$	$\Delta\ell_\delta = 1.620 \pm 0.036$	$\Delta\ell'_\delta = 7.157 \pm 0.29$
Transition region in ℓ-space	$\Delta\ell = (4.4)\Delta\ell_A = 4.84 \pm 0.31$				
Radius of interaction	$R = (7.5747 \pm 0.014) \times 10^{-13}$ cm				
Absorption parameter	$r_a = (1.390 \pm 0.003) \times 10^{-13}$ cm				
Nuclear radius	$R_n = r_a A^{1/3} = (5.3805 \pm 0.01) \times 10^{-13}$ cm				
Nuclear-surface thickness	$\Delta R = (1.49 \pm 0.08) \times 10^{-13}$ cm				
Total reaction cross section: $\sigma_R = 1.63$ b.					

Table XIV. Experimental results:[26]
α - Fe^{58}; E_{lab} = 64.5 MeV.

$\theta_{c.m.}$ (deg)	σ/σ_R	Error (%)	$\theta_{c.m.}$ (deg)	σ/σ_R	Error (%)
10.36	0.2501	0.3	23.20	0.13021	0.16
11.02	0.2553	0.3	24.09	0.061954	0.09
11.6	0.29835	0.35	25.41	0.004359	0.02
12.1	0.34435	0.4	26.46	0.038127	0.06
12.69	0.3821	0.45	27.77	0.12177	0.1
13.22	0.4129	0.4	29.09	0.17864	0.2
13.71	0.4123	0.4	32.24	0.050158	0.07
14.26	0.3799	0.4	33.63	0.009515	0.04
14.82	0.3280	0.36	35.44	0.0495	0.1
15.42	0.2609	0.3	37.54	0.10647	0.14
15.93	0.1768	0.24	38.64	0.09798	0.15
16.49	0.1113	0.2	40.07	0.05507	0.1
16.75	0.076557	0.15	42.11	0.01716	0.04
17.45	0.04655	0.1	45.92	0.06565	0.08
18.08	0.055225	0.1	48.51	0.04784	0.1
18.47	0.082771	0.1	51.25	0.02217	0.2
19.47	0.1694	0.18	54.41	0.04844	0.16
20.32	0.23761	0.6	59.11	0.02697	0.4
21.10	0.26173	0.26	60.74	0.02226	0.3
22.18	0.22469	0.17			

$Z = 26$, $E_{c.m.} = 58.2$ MeV, $\lambda = 0.308$f, $n = 2.067$, $v = 5.502 \times 10^9$ cm/sec.

Table XV. Theoretical analysis: α - Fe^{58}, E_{lab} = 64.5 MeV.

Best-fit parameters	$\ell_m = 22.036 \pm 0.026$	$\Delta\ell_A = 1.228 \pm 0.05$	$\delta = 1.38 \pm 0.008$	$\Delta\ell_\delta = 1.635 \pm 0.04$	$\Delta\ell'_\delta = 8.333 \pm 0.17$
Transition region in ℓ-space	$\Delta\ell = (4.4)\Delta\ell_A = 5.40 \pm 0.22$				
Radius of interaction	$R = (7.6140 \pm 0.008) \times 10^{-13}$ cm				
Absorption parameter	$r_a = (1.4007 \pm 0.002) \times 10^{-13}$ cm				
Nuclear radius	$R_n = r_a A^{1/3} = (5.422 \pm 0.007) \times 10^{-13}$ cm				
Nuclear-surface thickness	$\Delta R = (1.66 \pm 0.07) \times 10^{-13}$ cm				
Total reaction cross section: $\sigma_R = 1.701$ b.					

Table XVI. Experimental results:[27]
He^3 - Sn: E_{lab} = 31.2 MeV.

$\theta_{c.m.}$ (deg)	σ/σ_R	$\theta_{c.m.}$ (deg)	σ/σ_R
12.7	0.994	33.1	0.532
13.7	1.03	34.5	0.479
14.7	1.07	35.1	0.464
15.8	1.10	37.2	0.403
17.8	1.15	39.2	0.362
18.9	1.17	41.2	0.300
20.2	1.09	43.7	0.260
21.2	1.06	46.3	0.227
22.2	1.04	46.7	0.218
24.3	0.999	52.8	0.140
26.3	0.901	54.9	0.122
29.7	0.707	56.9	0.112
31.0	0.654	60.9	0.033
32.4	0.574	61.6	0.0868

$Z = 50$, $E_{c.m.} = 29.9$ MeV, $\lambda = 0.48$f, $n = 4.94$, $v = 4.428 \times 10^9$ cm/sec.

Table XVII. Theoretical analysis: He^3 - Sn, E_{lab} = 31.2 MeV.

Best-fit parameters	$\ell_m = 12.085 \pm 0.22$	$\Delta\ell_A = 1.33 \pm 0.13$	$\delta = 1.185 \pm 0.02$	$\Delta\ell_\delta = 2.816 \pm 0.3$	$\Delta\ell'_\delta = 18.34 \pm 1.10$
Transition region in ℓ-space	$\Delta\ell = (4.4)\Delta\ell_A = 5.85 \pm 0.57$				
Radius of interaction	$R = (9.00 \pm 0.10) \times 10^{-13}$ cm				
Absorption parameter	$r_a = (1.362 \pm 0.02) \times 10^{-13}$ cm				
Nuclear radius	$R_n = r_a A^{1/3} = (6.694 \pm 0.098) \times 10^{-13}$ cm				
Nuclear-surface thickness	$\Delta R = (2.26 \pm 0.24) \times 10^{-13}$ cm				
Total reaction cross section: $\sigma_R = 1.428$ b.					

Table XVIII. Experimental results:[27]
He^3 - Cu; E_{lab} = 31.2.

$\theta_{c.m.}$ (deg)	σ/σ_R	$\theta_{c.m.}$ (deg)	σ/σ_R
11.6	1.02	32.6	0.174
13.0	0.959	34.2	0.172
15.1	0.748	34.7	0.169
16.1	0.676	38.3	0.134
17.1	0.620	38.9	0.125
18.2	0.572	42.5	0.0784
19.2	0.524	43.0	0.0733
22.3	0.438	46.6	0.0665
23.2	0.387	50.8	0.0604
23.8	0.369	51.9	0.0590
25.9	0.325	54.9	0.0365
26.7	0.294	55.4	0.0325
27.9	0.251	59.0	0.0253
30.0	0.198	59.5	0.0252
30.7	0.184		

$Z = 29$, $E_{c.m.} = 29.3$ MeV, $\lambda\!\!\!^{-} = 0.498$f, $n = 2.86$, $v = 4.3 \times 10^9$ cm/sec.

Table XIX. Theoretical analysis: He^3 - Cu, E_{lab} = 31.2 MeV.

Best-fit parameters	$\ell_m = 12.42 \pm 0.12$	$\Delta\ell_A = 1.411 \pm 0.077$	$\delta = 1.176 \pm 0.011$	$\Delta\ell_\delta = 2.319 \pm 0.117$	$\Delta\ell'_\delta = 14.73 \pm 1.00$
Transition region in ℓ-space	$\Delta\ell = (4.4)\Delta\ell_A = 6.08 \pm 0.34$				
Radius of interaction	$R = (7.9885 \pm 0.05) \times 10^{-13}$ cm				
Absorption parameter	$r_a = (1.424 \pm 0.2) \times 10^{-13}$ cm				
Nuclear radius	$R_n = r_a A^{1/3} = (5.6817 \pm 0.08) \times 10^{-13}$ cm				
Nuclear-surface thickness	$\Delta R = (2.69 \pm 0.3) \times 10^{-13}$ cm				
Total reaction cross section: $\sigma_R = 1.336$ b.					

Table XX. Experimental results:[27]
He^3 - Al; E_{lab} = 31.2 MeV.

$\theta_{c.m.}$ (deg)	σ/σ_R	$\theta_{c.m.}$ (deg)	σ/σ_R
14.9	0.622	38.2	0.140
16.0	0.510	40.4	0.208
18.2	0.299	42.4	0.232
19.3	0.249	43.7	0.236
20.4	0.225	44.6	0.221
21.7	0.260	45.9	0.194
22.9	0.327	46.9	0.178
24.0	0.400	48.0	0.129
26.2	0.482	48.9	0.0968
27.2	0.439	51.2	0.0374
28.3	0.404	52.2	0.0342
29.5	0.336	53.4	0.0354
30.6	0.304	55.4	0.0542
31.7	0.199	58.6	0.0929
32.6	0.149	61.8	0.0881
34.9	0.0646	64.0	0.0752
35.8	0.0627	65.0	0.0620
37.0	0.0698	67.2	0.0336
37.2	0.0925	68.1	0.0333

$Z = 13$, $E_{c.m.} = 27.6$ MeV, $\lambda = 0.528f$, $n = 1.28$, $v = 4.43 \times 10^9$ cm/sec.

Table XXI. Theoretical analysis: He^3 - Al^{27}, E_{lab} = 31.2 MeV.

Best-fit parameters	$\ell_m = 10.54 \pm 0.06$	$\Delta\ell_A = 1.165 \pm 0.05$	$\delta = 1.096 \pm 0.014$	$\Delta\ell_\delta = 1.296 \pm 0.12$	$\Delta\ell'_\delta = 10.019 \pm 0.28$
Transition region in ℓ-space	$\Delta\ell = (4.4)\Delta\ell_A = 5.13 \pm 0.22$				
Radius of interaction	$R = (6.5493 \pm 0.63) \times 10^{-13}$ cm				
Absorption parameter	$r_a = (1.416 \pm 0.011) \times 10^{-13}$ cm				
Nuclear radius	$R_n = r_a A^{1/3} = (4.248 \pm 0.033) \times 10^{-13}$ cm				
Nuclear-surface thickness	$\Delta R = (2.69 \pm 0.5) \times 10^{-13}$ cm				
Total reaction cross section: $\sigma_R = 1.33$ b.					

Table XXII. Experimental results:[28]

d - Pb; E_{lab} = 15.0 MeV.

$\theta_{c.m.}$ (deg)	σ/σ_R	$\theta_{c.m.}$ (deg)	σ/σ_R
18.916	1.0	56.700	0.584
21.450	1.10	59.20	0.534
26.483	1.15	61.716	0.503
29.00	1.12	64.233	0.493
31.533	1.02	66.733	0.489
34.050	0.97	69.250	0.448
36.566	0.99	71.750	0.426
39.083	0.944	74.250	0.410
41.600	0.904	76.766	0.386
44.116	0.869	79.266	0.346
46.633	0.806	81.766	0.309
49.150	0.779	84.266	0.246
51.666	0.703	86.766	0.263
54.183	0.671	89.266	0.254

$Z = 82$, $E_{c.m.} = 14.6$ MeV, $\lambda = 0.84$f, $n = 4.76$, $v = 3.77 \times 10^9$ cm/sec.

Table XXIII. Theoretical analysis: d - Pb, E_{lab} = 15.0 MeV.

Best-fit parameters	$\ell_m = 5.25 \pm 0.17$	$\Delta\ell_A = 1.25 \pm 0.15$	$\delta = 1.059 \pm 0.047$	$\Delta\ell_\delta = 2.894$	$\Delta\ell'_\delta = 10.513$
Transition region in ℓ-space	$\Delta\ell = (4.4)\Delta\ell_A = 5.50 \pm 0.66$				
Radius of interaction	$R = (10.326 \pm 0.112) \times 10^{-13}$ cm				
Absorption parameter	$r_a = (1.380 \pm 0.019) \times 10^{-13}$ cm				
Nuclear radius	$R_n = r_a A^{1/3} = (8.176 \pm 0.113) \times 10^{-13}$ cm				
Nuclear-surface thickness	$\Delta R = (3.59 \pm 0.44) \times 10^{-13}$ cm				
Total reaction cross section: $\sigma_R = 1.166$ b.					

Table XXIV. Experimental results:[29]
d - Au^{197}; E_{lab} = 12.8 MeV.

$\theta_{c.m.}$ (deg)	σ/σ_R	$\theta_{c.m.}$ (deg)	σ/σ_R
14.333	1.02	59.683	0.730
17.367	0.990	62.700	0.670
20.4	1.01	65.700	0.640
23.4	0.980	68.733	0.620
26.433	0.980	73.733	0.580
29.467	1.01	78.766	0.520
32.500	0.990	83.783	0.480
35.533	0.980	88.800	0.430
38.533	0.990	93.783	0.430
41.566	0.950	108.75	0.380
44.600	0.900	113.733	0.360
47.600	0.840	118.700	0.360
50.633	0.830	123.667	0.320
53.667	0.810		

$Z = 79$, $E_{c.m.} = 12.5$ MeV, $\lambda = 0.915$f, $n = 4.96$, $v = 3.48 \times 10^9$ cm/sec.

Table XXV. Theoretical analysis: d - Au^{197}, E_{lab} = 12.8 MeV.

Best-fit parameters	$\ell_m = 3.28 \pm 0.1$	$\Delta\ell_A = 1.86 \pm 0.10$	$\delta = 0.578$	$\Delta\ell_\delta = 2.672 \pm 0.11$	$\Delta\ell'_\delta = 2.50 \pm 0.21$
Transition region in ℓ-space	$\Delta\ell = (4.4)\Delta\ell_A = 8.18 \pm 0.44$				
Radius of interaction	$R = (10.229 \pm 0.057) \times 10^{-13}$ cm				
Absorption parameter	$r_a = (1.388 \pm 0.01) \times 10^{-13}$ cm				
Nuclear radius	$R_n = r_a A^{1/3} = (8.079 \pm 0.058) \times 10^{-13}$ cm				
Nuclear-surface thickness	$\Delta R = (4.55 \pm 0.25) \times 10^{-13}$ cm				
Total reaction cross section: $\sigma_R = 1.04$ b.					

Table XXVI. Experimental results:[28]

d - W; E_{lab} = 15.0 MeV.

$\theta_{c.m.}$ (deg)	σ/σ_R	$\theta_{c.m.}$ (deg)	σ/σ_R
20.21	1.10	58.033	0.511
22.75	1.07	60.5333	0.456
25.26	1.04	63.05	0.414
27.80	1.08	65.566	0.398
30.3166	1.03	68.0666	0.384
32.85	0.951	70.5829	0.348
35.366	0.957	73.0833	0.330
37.883	0.891	75.600	0.292
40.400	0.836	78.10	0.272
42.950	0.801	80.6166	0.257
45.433	0.747	83.1166	0.249
47.966	0.656	85.6166	0.231
50.483	0.614	88.133	0.228
53.00	0.554	90.633	0.218
55.516	0.529		

$Z = 74$, $E_{c.m.} = 14.6$ MeV, $\lambda = 0.846$f, $n = 4.30$, $v = 3.76 \times 10^9$ cm/sec.

Table XXVII. Theoretical analysis: d - W, E_{lab} = 15.0 MeV.

Best-fit parameters	$\ell_m = 5.546 \pm 0.27$	$\Delta\ell_A = 1.22 \pm 0.30$	$\delta = 1.02$	$\Delta\ell_\delta = 2.253$	$\Delta\ell'_\delta = 8.941$
Transition region in ℓ-space	$\Delta\ell = (4.4)\Delta\ell_A = 5.37 \pm 1.32$				
Radius of interaction	$R = 10.00 \times 10^{-13}$ cm				
Absorption parameter	$r_a = (1.380 \pm 0.016) \times 10^{-13}$ cm				
Nuclear radius	$R_n = r_a A^{1/3} = (7.852 \pm 0.09) \times 10^{-13}$ cm				
Nuclear-surface thickness	$\Delta R = (3.71 \pm 0.95) \times 10^{-13}$ cm				
Total reaction cross section: $\sigma_R = 1.267$ b.					

Table XXVIII. Experimental results:[28]

d - Ta; E_{lab} = 15.0 MeV.

$\theta_{c.m.}$ (deg)	σ/σ_R	$\theta_{c.m.}$ (deg)	σ/σ_R
18.950	1.07	56.766	0.473
21.483	1.13	59.283	0.453
24.00	1.11	61.800	0.421
26.533	1.09	64.300	0.407
29.050	1.05	66.8166	0.380
31.566	0.903	69.3166	0.349
34.100	0.858	71.833	0.320
36.6166	0.782	74.333	0.292
39.133	0.762	76.850	0.276
41.66	0.733	79.350	0.261
44.183	0.649	81.8666	0.248
46.700	0.605	84.3666	0.237
49.2166	0.577	86.883	0.230
51.750	0.525	89.383	0.221
54.250	0.499		

$Z = 72$, $E_{c.m.} = 14.6$ MeV, $\lambda = 0.846$f, $n = 4.24$, $v = 3.76 \times 10^9$ cm/sec.

Table XXIX. Theoretical analysis: d - Ta, E_{lab} = 15.0 MeV

Best-fit parameters	ℓ_m = 5.741 ± 0.25	$\Delta\ell_A$ = 1.18 ± 0.29	δ = 1.045 ± 0.07	$\Delta\ell_\delta$ = 3.018 ± 0.27	$\Delta\ell'_\delta$ = 7.257 ± 1.04
Transition region in ℓ-space	$\Delta\ell = (4.4)\Delta\ell_A = 5.19 \pm 1.28$				
Radius of interaction	$R = (9.963 \pm 0.02) \times 10^{-13}$ cm				
Absorption parameter	$r_a = (1.381 \pm 0.03) \times 10^{-13}$ cm				
Nuclear radius	$R_n = r_a A^{1/3} = (7.813 \times 10^{-13})$ cm				
Nuclear-surface thickness	$\Delta R = (3.64 \pm 0.05) \times 10^{-13}$ cm				
Total reaction cross section: σ_R = 1300 b.					

Table XXX. Experimental results:[28]

d - Er; E_{lab} = 15.0 MeV.

$\theta_{c.m.}$ (deg)	σ/σ_R	$\theta_{c.m.}$ (deg)	σ/σ_R
20.233	1.07	58.0666	0.404
22.7666	1.05	60.583	0.370
25.283	1.00	63.10	0.332
27.8166	1.03	65.6166	0.326
30.333	0.970	68.133	0.302
32.850	0.890	70.633	0.278
35.383	0.830	73.150	0.254
37.90	0.80	75.650	0.238
40.422	0.735	78.1666	0.211
42.950	0.675	80.666	0.199
45.483	0.577	83.1666	0.193
48.00	0.520	85.666	0.184
50.5166	0.460	88.1666	0.173
53.0333	0.439	90.666	0.167
55.550	0.414		

$Z = 68$, $E_{c.m.} = 14.6$ MeV, $\lambda\!\!\!^{-} = 0.847$f, $n = 3.95$, $v = 3.76 \times 10^9$ cm/sec.

Table XXXI. Theoretical analysis: d - Er, E_{lab} = 15.0 MeV.

Best-fit parameters	ℓ_m = 6.05 ± 0.23	$\Delta\ell$ = 1.30 ± 0.23	δ = 0.9517	$\Delta\ell_\delta$ = 1.612 ± 0.087	$\Delta\ell'_\delta$ = 5.216 ± 1.01
Transition region in ℓ-space	$\Delta\ell = (4.4)\Delta\ell_A = 5.71 \pm 1.01$				
Radius of interaction	$R = (9.8107 \pm 0.17) \times 10^{-13}$ cm				
Absorption parameter	$r_a = (1.390 \pm 0.03) \times 10^{-13}$ cm				
Nuclear radius	$R_n = r_a A^{1/3} = (7.660 \pm 0.17) \times 10^{-13}$ cm				
Nuclear-surface thickness	$\Delta R = (4.15 \pm 0.74) \times 10^{-13}$ cm				

Total reaction cross section: σ_R = 1.477 b.

Table XXXII. Experimental results:[28]

d - Ag; E_{lab} = 15.0 MeV.

$\theta_{c.m.}$ (deg)	σ/σ_R	$\theta_{c.m.}$ (deg)	σ/σ_R
19.666	1.01	57.683	0.279
22.216	0.998	60.2166	0.254
24.766	0.835	62.750	0.229
27.30	0.695	65.2666	0.213
29.833	0.629	67.783	0.200
32.366	0.569	70.300	0.188
34.9166	0.530	72.8166	0.197
37.450	0.510	75.333	0.187
39.983	0.476	77.833	0.182
42.5166	0.437	80.333	0.174
45.050	0.393	82.833	0.167
47.583	0.355	85.350	0.152
50.1166	0.326	87.850	0.140
52.650	0.310	90.350	0.125
55.1666	0.296		

$Z = 47$, $E_{c.m.} = 14.5$ MeV, $\lambda = 0.853$f, $n = 2.73$, $v = 3.76 \times 10^9$ cm/sec.

Table XXXIII. Theoretical analysis: d - Ag, E_{lab} = 15.0 MeV.

Best-fit parameters	$\ell_m = 6.66 \pm 0.11$	$\Delta\ell_A = 0.69 \pm 0.03$	$\delta_0 = 1.08$	$\Delta\ell_\delta = 1.11 \pm 0.1$	$\Delta\ell'_\delta = 3.70 \pm 0.33$
Transition region in ℓ-space	$\Delta\ell = (4.4)\Delta\ell_A = 3.05 \pm 0.13$				
Radius of interaction	$R = (8.850 \pm 0.085) \times 10^{-13}$ cm				
Absorption parameter	$r_a = (1.407 \pm 0.018) \times 10^{-13}$ cm				
Nuclear radius	$R_n = r_a A^{1/3} = (6.699 \pm 0.11) \times 10^{-13}$ cm				
Nuclear-surface thickness	$\Delta R = (2.43 \pm 0.1) \times 10^{-13}$ cm				

Total reaction cross section: $\sigma_R = 1.437$ b.

Table XXXIV. Summary of results for r_a and ΔR.

Target \ Projectile	Absorption parameter r_a (10^{-13} cm)				Nuclear-surface thickness ΔR (10^{-13} cm)			
	Heavy ions	α-particles	He^3-ions	Deuterons	Heavy ions	α particles	He^3-ions	Deuterons
Pb^{208}	1.388± 0.008 1.383± 0.01				2.85± 0.2 2.35± 0.3			
Pb(nat)		1.383± 0.01		1.3804± 0.019		1.74± 0.1		3.59± 0.49
Au				1.388 ± 0.01				4.55± 0.25
W				1.380 ± 0.016				3.71± 0.9
Ta	1.382± 0.018			1.381 ± 0.03	2.52± 0.36			3.64± 0.05
Er				1.390 ± 0.03				4.15± 0.7
Sn			1.362± 0.02				2.26± 0.24	
Ag	1.379± 0.023			1.407± 0.018	2.2 ± 0.36			2.43± 0.1
Cu			1.424± 0.02				2.96± 0.3	
Ni		1.390± 0.003				1.49± 0.08		
Fe		1.40 ± 0.002				1.66± 0.07		
Al			1.416± 0.01				2.69± 0.05	

$R_{O^{16}} = (3.497 \pm 0.03) \times 10^{-13}$ cm; $R_a = 2.192 \times 10^{-13}$ cm; $R_{He^3} = 2.3 \times 10^{-13}$ cm.

$R_{C^{12}} = (3.162 \pm 0.03) \times 10^{-13}$ cm; $R_d = 2.15 \times 10^{-13}$ cm.

Furthermore, a comparison between pairs of C^{12} - Ta and d - Ta, C^{12} - Ag and d - Ag, and C^{12} - Pb and d - Pb systems yielded an average deuteron radius of

$$R_d = 2.15 \times 10^{-13} \text{ cm} .$$

The radius of He^3-ions was taken to be 2.3×10^{-13} cm.[31] Finally Table XXXV presents the results for the total reaction cross section.

1. Discussion of Results

The average absorption parameter was calculated to be

$$\bar{r}_a = (1.389 \pm 0.018) \times 10^{-13} \text{ cm} .$$

The maximum deviation from this value is 0.03×10^{-13} cm and the average deviation is 0.018. Apparently the simple $A^{1/3}$ law for the nuclear radius holds very well. Consequently, no information concerning the nuclear structure can be obtained from this study of nuclear radii. Such characteristics as closed shells (Pb^{208}, Sn) and quadrupole deformations (Ta, Er) seem to have no apparent influence on R_n.

On the other hand, there seems to be an extraordinary diversity in the values of the surface thickness, ΔR, of the target nucleus for the various projectiles employed. It is suggested that the nonuniformity in ΔR, even for the same target nucleus (Pb, Ta, Ag), is entirely due to the projectile. The ΔR's obtained in the case of heavy ions reflect the fact that the projectile itself possesses a diffuse surface. The large ΔR's in the case of deuteron and He^3-ion scattering indicate that these particles are very loosely bound systems which are strongly polarized by the strong Coulomb force as they approach the target nucleus. One expects then that these projectiles will start breaking up, thus removing themselves from the entrance channel even before they can enter the fringes of the nuclear distribution of the target. This argument becomes plausible if we consider the fact that the Coulomb barrier, which does not affect the motion of the neutron, is about 12 MeV in the case of Au^{197}, for example, whereas the binding energy of the deuteron is only 2.23 MeV, and that for He^3 is about 2.7 MeV/nucleon. The result is an apparent large ΔR. On the other hand, the α particle, being a tightly

Table XXXV. Total reaction cross sections

System	$E_{c.m.}$ (MeV)	σ_R (barns)	System	$E_{c.m.}$ (MeV)	σ_R (barns)
O^{16} - Pb^{208}	158.0	2.520	He^3 - Cu	29.257	1.638
C^{12} - Pb^{208}	118.395	2.237	He^3 - Al	27.564	1.336
C^{12} - Ta^{181}	114.675	2.227	d - Pb	14.659	1.166
C^{12} - Ag	110.035	2.118	d - Au	12.525	1.046
α - Pb	46.323	1.939	d - W	14.64	1.267
α - Ni^{58}	58.547	1.635	d - Ta	14.639	1.300
a - Fe^{58}	58.725	1.701	d - Er	14.625	1.477
He^3 - Sn	29.882	1.428	d - Ag	14.530	1.437

bound unit, appears to be the most realistic probe of the nuclear-surface thickness. This is brought out by a check of the sensitivity functions that appear in Figs. 32, 33, 34, and 35. For α particles, the sensitivity of σ/σ_R to the parameter $\Delta\ell_A$, which is a measure of ΔR, is about 75%, 80%, and 10% greater than for deuterons, He^3-ions, and heavy ions, respectively.

For a given projectile, however, variations in ΔR appear to agree qualitatively with our knowledge of the structure of the various target nuclei. Deformed nuclei, for example, due to their random orientation, are expected to yield an apparent surface thickness which is larger than the real one by roughly the difference between the two semi-axes. Tantalum, tungsten, and erbium verify this prediction. In the case of C^{12} scattering, the ΔR for tantalum is larger than that of either Pb^{208} or Ag. In the case of deuteron scattering, the ΔR's for these three nuclides are significantly larger than the ΔR's for the nondeformed Pb and Ag. On the other hand, nuclei with closed shells appear to possess a smaller ΔR, as is evidenced by the results for Pb, Sn, and Ni.

2. Accuracy of Results

The accuracy and uniqueness of the stated results were given primary consideration throughout the data analysis. The experimental

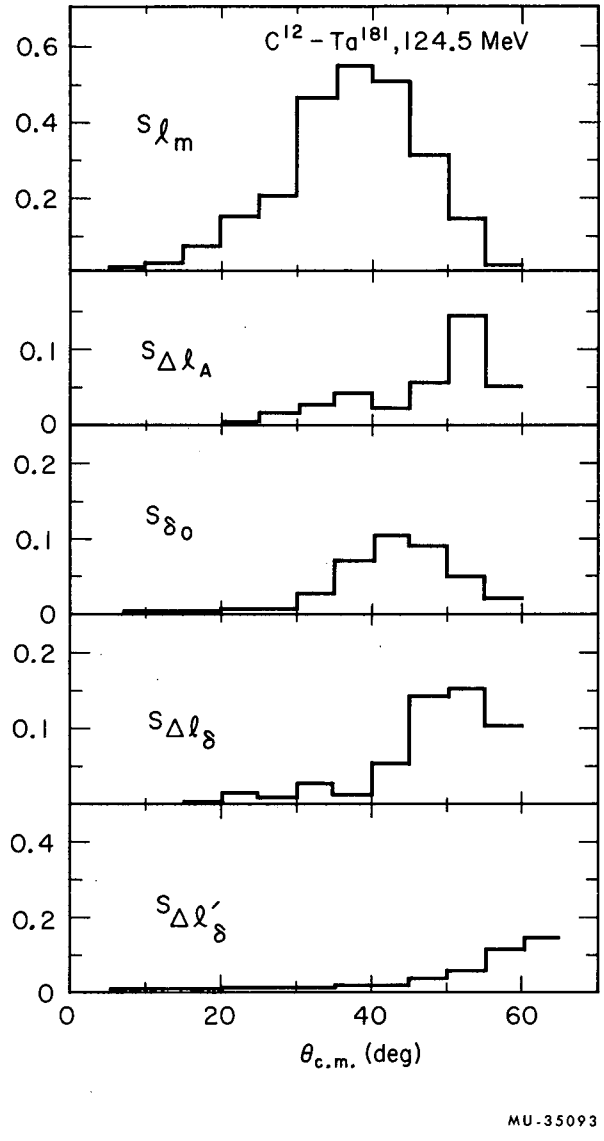

Fig. 32. Sensitivity, S, of σ/σ_R to the parameters ℓ_m, $\Delta\ell_A$, δ_0, $\Delta\ell_\delta$, and $\Delta\ell'_\delta$ for C^{12} - Ta^{181}.

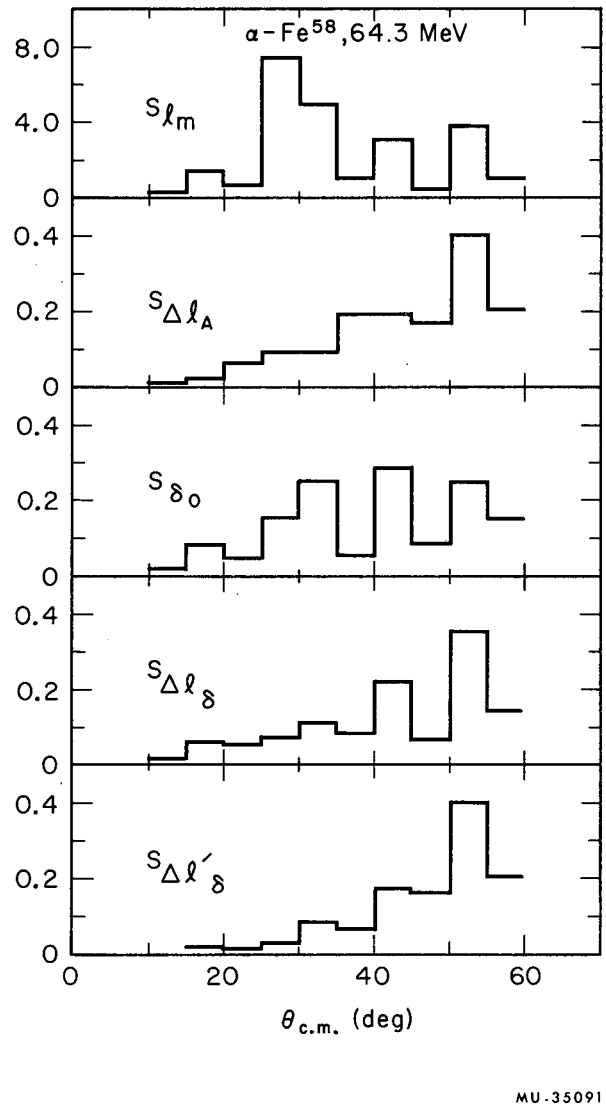

Fig. 33. Sensitivity, S, of σ/σ_R to the parameters ℓ_m, $\Delta\ell_A$, $\Delta\ell_\delta$, and $\Delta\ell'_\delta$ for α - Fe^{58}.

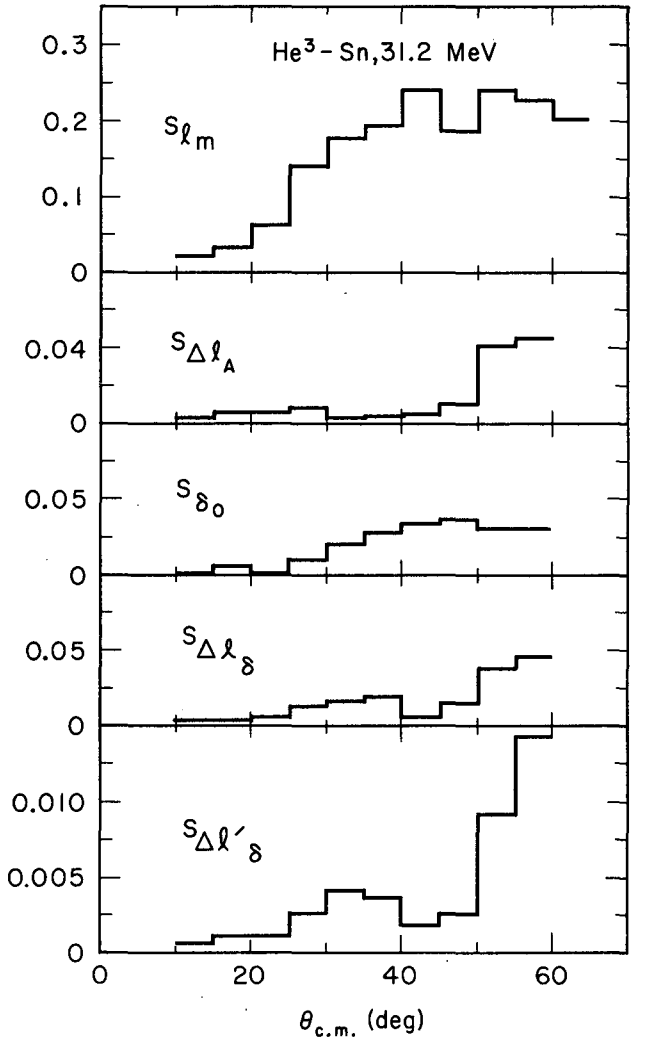

MU-35090

Fig. 34. Sensitivity, S, of σ/σ_R to the parameters ℓ_m, $\Delta\ell_A$, δ_0, $\Delta\ell_\delta$, and $\Delta\ell'_\delta$ for He^3 - Sn.

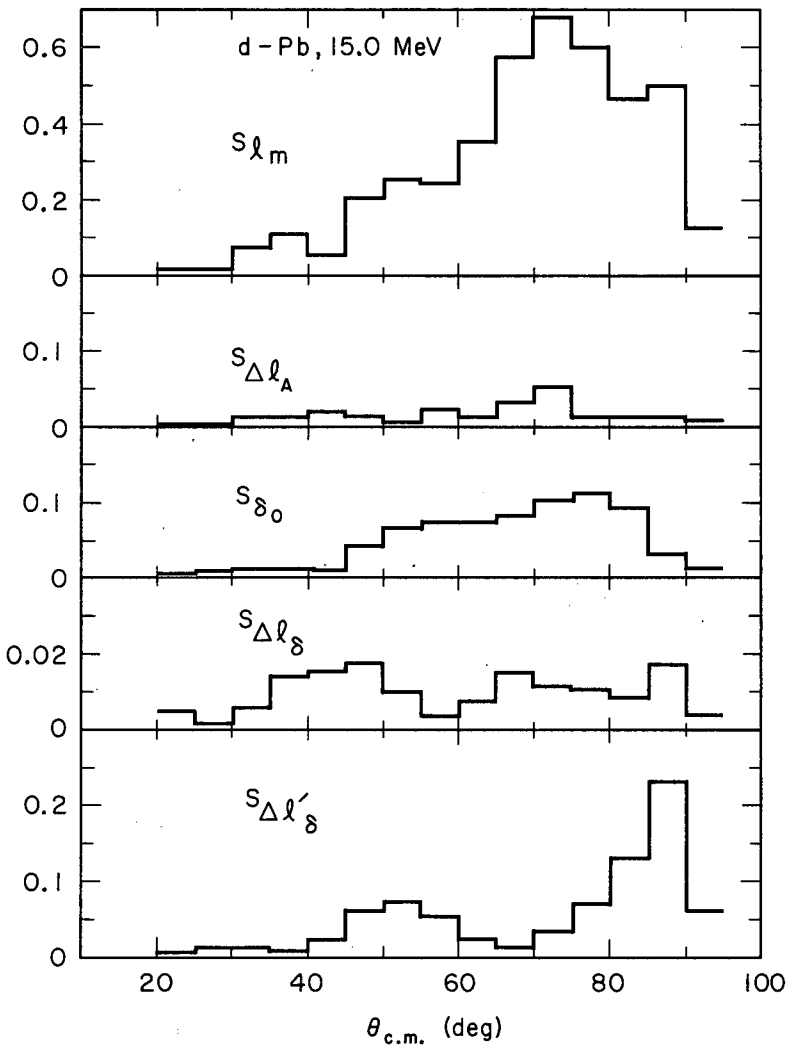

Fig. 35. Sensitivity, S, of σ/σ_R to the parameters ℓ_m, $\Delta\ell_A$, δ_0, $\Delta\ell_\delta$, and $\Delta\ell'_\delta$ for d - Pb.

values of σ/σ_R were weighted by the experimental errors during the curve-fitting process, thus producing a better fit for the points with smaller errors. The stated uncertainties to the best-fit parameters cover the range over which these parameters could change without affecting the goodness of fit. An attempt was made to determine whether other sets of "best-fit" parameters exist outside this range that could produce the same goodness of fit as measured by χ^2. The agreement between the normal equations and the calculated correlation between the parameter (see Sec. II.F), as well as the value of χ^2, served as guides in this investigation. The results are as follows:

a. Heavy ions. Insufficient data at large angles made the electronic computer unable to decide upon the proper value for the parameter $\Delta\ell'_\delta$, which ranged from about 10 to 40 without affecting appreciably the value of χ^2. At the same time the other parameters varied as much as 10 to 15%. Figure 32 which shows the sensitivity function for the case of C^{12} - Ta and is typical of the heavy-ion cases, indicates that the elusive parameter $\Delta\ell'_\delta$ begins to become influential at angles beyond $\theta_{c.m.} = 40$ deg. Unfortunately the available data does not extend beyond 35 deg. A set of "best-fit" parameters was then chosen and employed to calculate values of σ/σ_R for $\theta_{c.m.} > 40$ deg. These calculated "data" together with the experimental data were fed into the computer, which then readily could pick a set of "best-fit" parameters. This made apparent the need for data at nonforward angles. In order to overcome this difficulty the available data were reweighted so that heavier weights were assigned to the forward angles, where σ/σ_R is sensitive to ℓ_m and, to a lesser degree, to $\Delta\ell_A$. Since the correlation between ℓ_m and $\Delta\ell_A$ on one hand, and $\Delta\ell_\delta$ on the other is not negligible, determination of ℓ_m and $\Delta\ell_A$ makes the choice of $\Delta\ell'_\delta$ much easier. Under these circumstances, the computer was able to find a set of best-fit parameters. Since there is a small, although inconclusive, indication that the radius of interaction may depend on the scattering angle,[30] the uniqueness of the results in the case of heavy ions to about 2.8% for r_a and about 15% for ΔR cannot be verified until sufficient data at nonforward angles becomes available.

b. α Particles and He^3 ions. The stated uncertainties in Table XXXIV cover sufficiently the possible sets of "best-fit" parameters. These data were the easiest to fit because in most cases they have sufficient structure to insure low correlation among the parameters.

c. Deuterons. The practically structureless form of the deuteron data made the fitting process quite difficult. An initial investigation pointed to the possible range for the parameter δ_0. This parameter was then fixed at values varying by small increments, over this range. This process resulted in definite sets of "best-fit" parameters for Ta, W, and Er. For Au, Ag, and Pb, in addition to δ_0, $\Delta\ell_A$ had to be scanned over a range of optimum values and then kept fixed. The possibility for multiple sets in these cases is evident. However, the stated uncertainty of the parameters for Ta, W, and Er covers the possible "best-fit" sets. On the other hand, a similar claim cannot be made for Au, Ag, and Pb.

It has been pointed out earlier that the values for the nuclear surface thickness ΔR, obtained in deuteron scattering, and to a lesser degree, in He^3-ion scattering, are unrealistically large. However, they indicate that, because of the strong Coulomb field, absorption for these projectiles starts before they enter the nuclear domain.

Calculations were performed by Hoffmann under the assumption that the deviation of the elastic differential cross section for deuterons, $(d\sigma/d\Omega)$, from the Rutherford cross section, $(d\sigma/d\Omega)_R$, was entirely due to the electric dipole breakup of the deuterons outside the target nucleus.[32] The Coulomb field was treated as a perturbation that induced an increase in the internal energy of the deuteron, and the minimum critical angle where the deviation of the $d\sigma/d\Omega$ from $(d\sigma/d\Omega)_R$ occurred was calculated. The laboratory energy of the incident deuterons was found to be 24 MeV. The predictions of this treatment agree well with the experimental data as shown in Table XXXVI.

If the above point of view is adopted, the symmetric form of the absorption amplitude A_ℓ becomes objectionable in the case of deuterons. If A_ℓ has to start decreasing to values smaller than unity for ℓ's that correspond to impact parameters larger than the nuclear radius and still be $A_{\ell_m} = 1/2$ at the nuclear radius, as the results of the present

Table XXXVI. Critical angle for elastically scattered deuterons.

Target	Energy (MeV)	Experimental critical angle (deg)	Calculated critical angle (deg)
Au	11.0	45	47.0
Au	21.6	13	13.3
Bi	11.0	49	50.7
Pb	15.2	26	25.7
Ta	11.0	40	42.0

analysis indicate, then because A_ℓ is symmetric about $\ell = \ell m$, the rate of its decrease within the nucleus should be smaller than that for α particles, for example. This clearly implies that the mean free path for deuterons within the nuclear matter is larger than that for an α particle. If one considers the difference in their binding energy, this conclusion is not realistic.

Finally, there is one further difficulty which, however, can be easily removed in any future work. Namely, if we assume electric breakup of the deuterons outside the target nucleus and that the correlation between absorption and the sign of the real nuclear phase shift (as discussed in Sec. II.E) is correct, δ_ℓ should start negative for large ℓ and remain negative down to $\ell = 0$. For this to be possible the parameter δ_0 should be allowed to go negative. Unfortunately the sign of δ_0 was restricted to be positive. This restriction is justified in the case of heavy ions and α particles. However, the results indicate that it may have an adverse effect on the results in the case of deuterons and He^3 ions. Furthermore, a high correlation coefficient between $\Delta\ell_A$--which measures ΔR--and δ_0 suggest the possibility of multiple sets for these two parameters. Finally, recent optical-model calculations[33] for 11- to 12-MeV deuterons elastically scattered by targets ranging from Ar to Sn produced negative phase shifts for four different "best-fit" optical potentials, for all partial waves.

3. Comparison with Other Results

Several methods have been tried in the past for determination of nuclear radii and the nuclear-surface thickness.

a. Charge sensitive methods, such as determination of Coulomb effects in mirror nuclei, μ-meson scattering and μ-mesonic atoms, and fine structure in x-ray spectra and isotope shifts, have yielded a value for the parameter r_a equal to 1.0 to 1.2×10^{-13} cm.

b. Range-of-nuclear-force methods such as low, high and super-high neutron scattering, proton scattering and α-particle scattering have yielded an r_a = 1.3 to 1.5×10^{-13} cm.

c. The extensive electron scattering experiments by R. Hofstadter[13] have produced an average $r_a = 1.23 \times 10^{-13}$ cm.

d. The optical-potential analysis of elastic scattering has yielded r_a = 1.18 to 1.35×10^{-13} cm for α-particle scattering.[34] The same 15.0-MeV deuteron data analyzed in the present work was also analyzed by means of an optical model.[35] At least three different sets of best-fit parameters were found. The results for Pb, W, Ta, Er, and Ag are given in Table XXXVII.

Table XXXVII. Optical-potential analysis of 15.0-MeV deuterons.[35]

Target	Total reaction cross section, σ_R (barns)	r_0 (Real) (10^{-13} cm)	r_a (Imaginary) (10^{-13} cm)
Pb	1.302	1.291	1.381
W	1.262	0.936	1.330
Ta	1.527	1.283	1.350
Er	1.456	0.961	1.363
Ag	1.518	1.471	1.368

The values for σ_R compare favorably with those obtained in the present work.

It should be pointed out, however, that the nuclear radii obtained by means of optical-potential calculations corresponds to the distance from

the center of the nucleus to the half-value of the nuclear potential, and consequently they differ by definition from the radii obtained by phase-shift analysis in the present work.

B. Inelastic Scattering.

The level scheme of Ta^{181}, Fig. 36, shows that a large fraction of the inelastic events corresponding to excitation of the ground-state rotational band accompanies the 136-keV transition from the first excited to the ground state. The figure shows only the lower members of the ground-state band and the 482-keV and 615-keV levels. Other low-lying states are not Coulomb-excited.[36] We may assume that Coulomb excitation for the 482- and 615-keV states is much weaker than that for the 303- and 136-keV states, since their observed lifetimes are long compared to those of the lower states. Therefore, it is a good approximation to assume that the yield of the 136-keV transition measures the major contribution of Coulomb excitation to the inelastic scattering that is not resolved in the spectra of scattered O^{16} ions.

Figure 37 shows the three relevant energy spectra at $\theta_{lab} = 20$ deg, which were obtained simultaneously in the course of the experiment. Here (a) is the spectrum of the scattered O^{16} ions, (b) is the spectrum of scattered ions in coincidence with γ-rays selected (by a single-channel analyzer "window") to include essentially all of the 136-keV and, unavoidably, some of the 167-keV gammas, and (c) is the spectrum of scattered ions in coincidence with all γ-rays. The inelastically scattered particles in coincidence with the selected γ-rays are concentrated under the elastic peak.

Under the further assumption that the γ-ray emission is isotropic, one calculates the ratio of inelastic to elastic scattering events by means of the expression

$$f = \frac{N_{inelastic}}{N_{elastic}} = \frac{4\pi}{\Omega} \frac{1}{m} (\alpha + 1) \frac{N_{(\gamma)}^{peak}}{N^{peak}} , \qquad (24)$$

where Ω is the solid angle of the NaI crystal, m is the γ-ray counting efficiency determined experimentally, N^{peak} is the number of events in

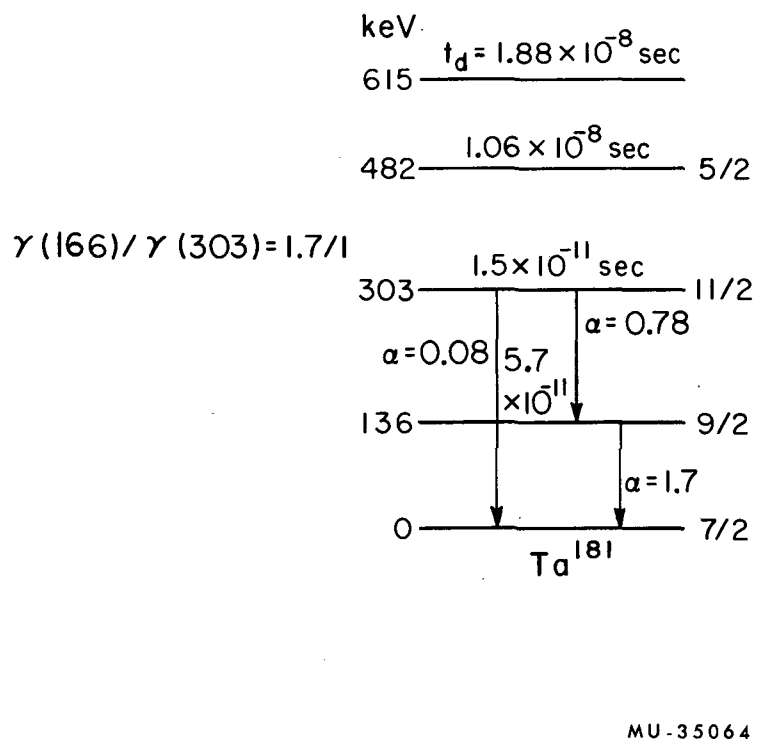

Fig. 36. Level scheme for Ta^{181}.

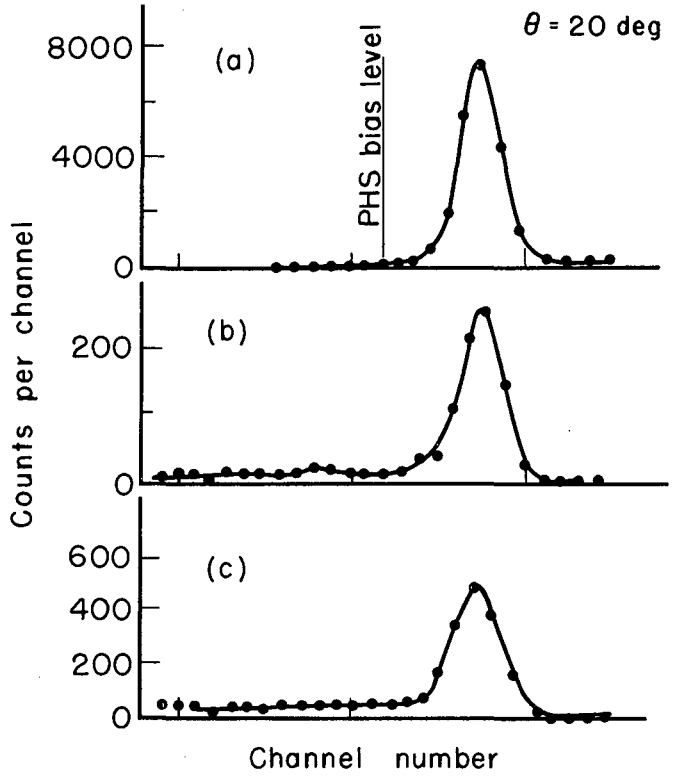

MU-35033

Fig. 37. Energy spectra obtained at $\theta_{lab} = 20$ deg during the course of the O^{16}-γ coincidence experiment on Ta^{181}. The O^{16} beam energy was 166 MeV, and the width at half maximum of the peaks shown is about 1.5 MeV. (a) All O^{16} ions. (b) O^{16} ions in coincidence with energy-selected γ-rays. (c) O^{16} ions in coincidence with all γ-rays.

the elastic peak, $N_{(\gamma)}^{peak}$ is the number of inelastic events in coincidence with the selected γ-rays, and α is the total conversion coefficient of the 136 state; $\alpha = 1.7$ in this case. Equation (24) is correct only when all the inelastic events correspond to excitation of the 136-keV state. However, the 136-keV γ-ray intensity is not very strongly dependent on the relative population of the rotational levels. Thus, if 77% of the inelastic events correspond to the first excited state and the rest to the second, as in the case of E2 Coulomb excitation, the value of f obtained is too high by about 10%. Similar spectra to those in Fig. 37 were obtained at six angles altogether. Table XXXVIII is a summary of the results. The number of accidental coincidences, N_{acc}^{peak}, was determined by means of independent measurements. Figure 38 shows a plot of f vs the scattering angle. The points are the experimental results. The curve is the sum of E2 Coulomb-excitation probabilities for the first and second rotational states of Ta^{181} obtained by means of semiclassical theoretical calculations.[20] The agreement between theory and experiment is quite good up to $\theta_{c.m.} = 25$ deg which corresponds to an angle just before the final rise in the curve of σ/σ_R versus angle. In this region of very forward angles, the inelastic contribution to the apparent elastic cross section appears to be 5 to 8%. Beyond $\theta_{c.m.} = 25$ deg, the experimental results deviate from the theoretical curve, and the inelastic contribution was determined to be as high as 28% of the elastic cross section. One may conclude, therefore, that: first, heavy-ion elastic scattering data should always be corrected for inelastic contributions especially for deformed nuclei with low-lying rotational states; and second, that the theoretically calculated Coulomb excitation correction may be applied accurately over the range of forward angles only.

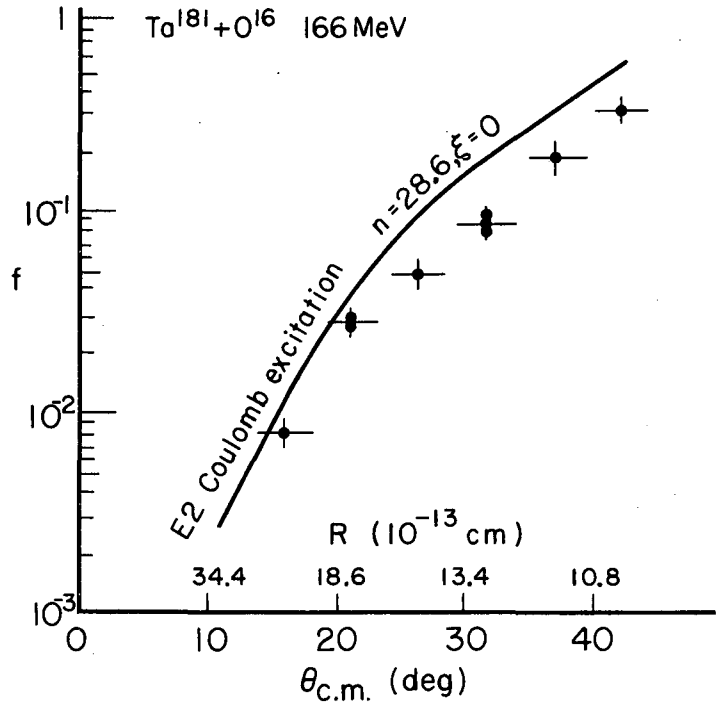

MU-35032

Fig. 38. Ratio, f, of inelastic to elastic scattering, as a function of scattering angle. R is the corresponding distance of closest approach on a Coulomb trajectory. The vertical bars represent uncertainty in f due to the NaI detector solid angle. Horizontal bars represent angular range covered by the silicon-detector aperture.

Table XXXVIII. Summary of results.

θ_{lab} (deg)	$\theta_{c.m.}$ (deg)	N^{peak}	$N(\gamma)^{peak}$	N_{acc}^{peak}	$\frac{N_{(\gamma)}^{peak}-N_{acc}^{peak}}{N^{peak}}$	f
15	16.3	267×10^3	201	115	0.32×10^{-3}	0.78×10^{-2}
20	21.7	558×10^3	745	128	1.11×10^{-3}	2.72×10^{-2}
		$1\,130\times10^3$	1840	654	1.05×10^{-3}	2.60×10^{-2}
25	27.2	54×10^3	125	23	1.9×10^{-3}	4.6×10^{-2}
30	32.6	97×10^3	392	100	3.0×10^{-3}	7.4×10^{-2}
		88×10^3	355	55	3.5×10^{-3}	8.6×10^{-2}
		281×10^3	1095	174	3.25×10^{-3}	8.0×10^{-2}
35	37.9	20.1×10^3	148	12	6.8×10^{-3}	16.6×10^{-2}
40	42.9	3.1×10^3	37	2	11.0×10^{-3}	28.0×10^{-2}

C. Applicability of the Diffraction Model in the Elastic $\pi^{\pm}p$ Scattering at very High Energies and Nonforward Angles

Recently, π^-p and π^+p elastic-scattering data have been published which show a secondary peaking of the elastic differential cross section $d\sigma/d\Omega$, in addition to the very forward diffraction peaking. The secondary peak is quite prominent in the π^-p data at 2.01 BeV/c and π^+p data at 2.02 BeV/c of Damouth et al.,[37] in the π^+p data at 1555 MeV of Helland,[38] in the π^-p data at 1.50 BeV of Chretien et al.,[39] and in the π^-p data at 1.59 BeV of Alitti et al.[40] The secondary peak in the π^+p data at 2.0 and 2.5 BeV/c of Cook et al.[41] is obscured by the fairly large statistical errors. Other data are quite inconclusive as to the existence of the peak.

The forward peak is well known to be due to diffraction of the partial waves. There is no general agreement however as to the nature of the secondary peak which occurs at $\cos\theta_{c.m.} = -0.5$ in the 1.50-BeV/c $\pi^- + p$ data, at $\cos\theta_{c.m.} = -0.2$ in the 1.59-BeV/c π^-p data, at $\cos\theta_{c.m.} = 0.2$ in the 2.01-BeV/c π^-p data, and at $\cos\theta_{c.m.} = 0.45$ in the 2.00-BeV/c π^+p data.

Damouth, Jones, and Pearl[37] have attempted to explain the secondary peak in their $\pi^- p$ data by associating it with the total $\pi^- p$ cross section maximum at 2.08 BeV/c. Simmons,[42] however, proposed that the secondary peak may very well be a second diffraction maximum. He performed calculations employing what essentially is the simple sharp-cutoff diffraction model which is described in Sec. II.B. of this work. He was able to reproduce the second maximum in $d\sigma/d\Omega$ both in position and magnitude, along with additional maxima and zeroes of the cross section which did not appear in the experimental data.

In the present work an attempt was made to fit the 2.01-BeV/c $\pi^- p$ elastic data by means of a partial-wave analysis that incorporates the parameterization outlined in Sec. II.E. Emphasis was placed especially upon the successful reproduction of the essential features of the secondary peak. Figure 39 shows the results of this investigation. The solid curve is the differential cross section $d\sigma/d\Omega$ calculated using the best-fit parameters $\ell_m = 3.0777$, $\Delta\ell_A = 2.562$, $\delta_0 = 0.251$, $\Delta\ell_\delta = 3.657$, and $\Delta\ell'_\delta = 0.1366$. The absorption amplitude A_ℓ was 90% of its maximum value at $\ell = 9$, which means that at least nine partial waves participate in the diffraction scattering. Note that the second peak in the cross section is fitted well both in magnitude and position.

It is very probable that the fit will improve further if the phase-shift analysis were refined sufficiently to include spin-flip scattering and the effect of having two total-angular-momentum states, $j = \ell \pm 1/2$, for every ℓ wave. However, these refinements are not worthwhile unless the data is considerably more accurate and more closely spaced than that which is available. The uncertainties, especially at large angles, are quite high, without even including an overall normalization error of $\pm 8\%$.

Applying the semiclassical condition, Eq. (10), we obtain a radius of interaction

$$R = 5.81 \times 10^{-13} \text{ cm}$$

for $\pi^- p$ scattering at 2.01 BeV. This radius is most likely to change with incident energy. Very recently, Perl and Corey[43] have made a phase-shift analysis of a considerable amount of $\pi^\pm p$ elastic-scattering

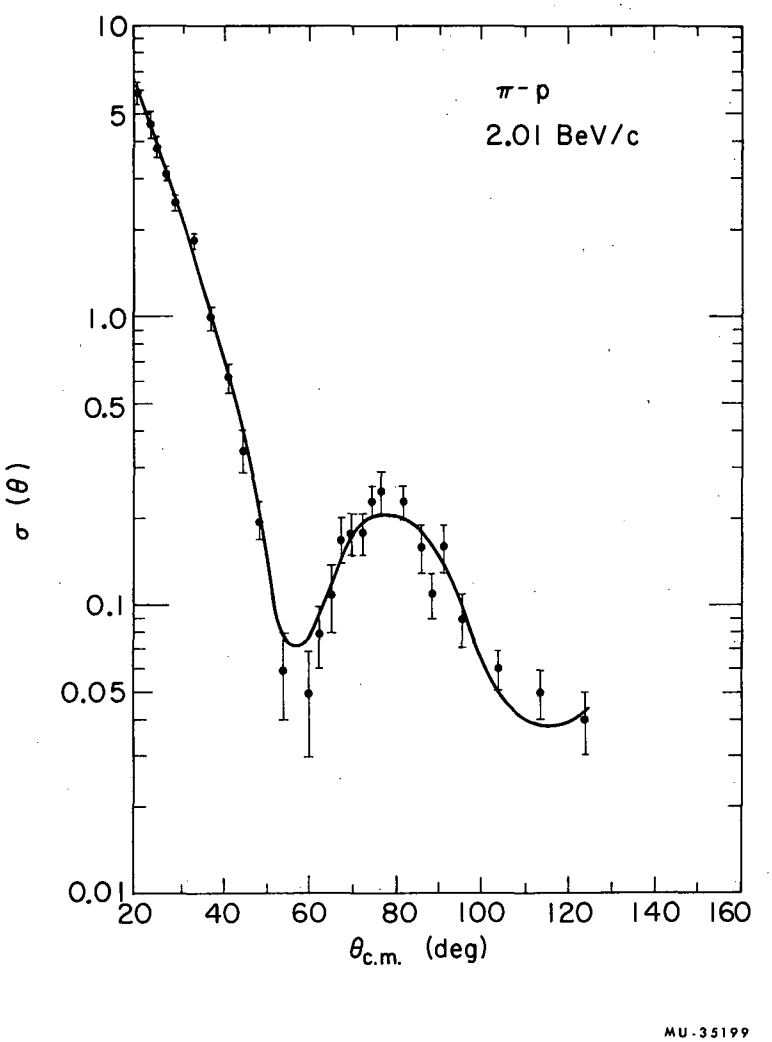

Fig. 39. Angular distribution of $\pi^- p$ elastic scattering at 2.01 BeV/c. The dots represent the experimental cross section, and the solid line is the calculated cross section with the values of the parameters as they appear in the text.

data at energies above 1 BeV/c. Their diffraction model is simpler than the one used in the present work in that they assume absorptive scattering only, i.e., they set all $\delta_\ell = 0$. Furthermore, instead of parameterizing the absorption amplitude A_ℓ, they allow a computer program to find directly the values of A_ℓ for every ℓ wave. Consequently the number of parameters used is equal to the maximum number of partial waves necessary to obtain a good fit to the data. This number ranged from four to eleven for the various sets of data.

Wherever a second peak was present in the experimental differential cross section ($\pi^- p$ at 1.50 BeV/c, 1.59 BeV/c, and 2.01 BeV/c; $\pi^+ p$ at 1.50 BeV/c, 1.55 BeV/c, and 2.0 BeV/c), it was reproduced in the calculated cross section. The fits to the data improved considerably when partial potential scattering was allowed. They were further improved when complete potential scattering was introduced by in effect making $\delta_\ell \neq 0$, and when a term was added to the differential cross section, which was supposed to account for spin-flip scattering.

The conclusions derived from the foregoing are (1) the phase shift analysis of the elastic high-energy $\pi^\pm p$ data is a simple but successful means of fitting this data, and (2) the important features of the second peak in the differential cross section are reproduced very well, thus enhancing the assumption that this peak is also due to diffraction of the partial waves.

ACKNOWLEDGMENTS

It is my very special pleasure to thank Dr. Homer E. Conzett who suggested the project. Dr. A. C. Helmholz provided invaluable guidance, support, and encouragement. I also thank Mrs. Claudette Rugge for her tireless help with the computer program, and Miss Miriam Machlis for her able assistance.

REFERENCES

1. G. Igo, H. E. Wegner, and R. M. Eisberg, Phys. Rev. 101, 1508 (1956).
2. J. A. McIntyre, S. D. Baker, and K. H. Wang, Phys. Rev. 125, 584 (1962).
3. J. A. McIntyre, S. D. Baker, and T. L. Watts, Phys. Rev. 116, 1212 (1959).
4. L. Schiff, Quantum Mechanics, Second Edition (McGraw-Hill, New York, 1955), p. 103.
5. J. S. Blair, Phys. Rev. 95, 1218 (1954).
6. J. M. Blatt and V. F. Weisskopf, Theoretical Nuclear Physics (John Wiley and Sons, New York, 1952), p. 325.
7. R. E. Ellis and L. Schecter, Phys. Rev. 99, 1044 (1955).
8. J. S. Blair, Phys. Rev. 108, 827 (1957).
9. J. A. McIntyre, K. H. Wang, and L. C. Becker, Phys. Rev. 117, 1337 (1960).
10. K. R. Greider and A. E. Glassgold, Ann. Phys. (New York) 10, 100 (1960).
11. W. E. Frahn and R. H. Venter, Ann. Phys. (New York) 24, 243 (1963).
12. D. A. Bromley, J. A. Kuehner, and E. Almquist, Phys. Rev. Letters 4, 365 (1960).
13. R. Hofstadter, Rev. Mod. Phys. 28, 214 (1956).
14. H. E. Conzett, A. Isoya, and E. Hadjimichael, in Proceedings of the Third Conference on Reactions between Complex Nuclei, A. Ghiorso, R. M. Diamond, and H. E. Conzett, Eds. (University of California Press, Berkeley, 1963).
15. F. B. Morinigo, Nucl. Phys. 36, 529 (1962).
16. C. H. Porter, Phys. Rev. 112, 1722 (1958).
17. R. H. Moore and R. K. Zeigler, Los Alamos Scientific Laboratory Report LA-2367, October 15, 1959 (unpublished).
18. I. S. Sokolnikoff and R. M. Redheffer, Mathematics of Physics and Modern Engineering (McGraw-Hill, New York, 1958) pp. 663-666.

19. A. Isoya, H. E. Conzett, E. Hadjimichael, and E. Shield, in Proceedings of the Third Conference on Reactions between Complex Nuclei, A. Ghiorso, R. M. Diamond, and H. E. Conzett, Eds. (University of California Press, Berkeley, 1963).
20. K. Alder, A. Bohr, T. Huus, B. Mottelson, and A. Winter, Rev. Mod. Phys. 28, 432 (1956).
21. E. L. Hubbard et al., Rev. Sci. Instr. 32, 621 (1961).
22. F. S. Goulding and W. L. Hansen, Nucl. Instr. Meth. 12 249 (1961).
23. S. D. Baker, Elastic Scattering of Light Nuclei by Heavy Nuclei, unpublished Ph. D. Thesis, Yale University, May 1963.
24. J. Alster and H. E. Conzett, Phys. Rev. 136, B1023 (1964).
25. R. E. Ellis, Lawrence Radiation Laboratory, private communication.
26. P. Darriulat, G. Igo, H. G. Pugh, J. R. Meriwether, and S. Yomabe, Phys. Rev. 134, B42 (1964).
27. J. G. Vidal, G. Igo, and S. S. Markowitz, in Chemistry Division Annual Report, Lawrence Radiation Laboratory Report UCRL-9506, 1960 (unpublished).
28. R. K. Jolly, E. K. Lin, and B. L. Cohen, Phys. Rev. 130, 2391 (1963).
29. L. Freindl, H. Niewodniezanski, J. Narzynski, M. Stapa, A. Strzatkowski, Institute of Nuclear Physics, Cracow, Report 203, August 1962.
30. D. D. Kerlee, J. S. Blair, and G. W. Farwell, Phys. Rev. 107, 1343 (1957).
31. Sergio DeBenedetti, Nuclear Interactions (John Wiley and Sons, New York, 1964).
32. Dennis G. Hoffman, The Elastic Scattering of 24-MeV Deuterons, Ph. D. Thesis, Lawrence Radiation Laboratory Report UCRL-9610, September 1960.
33. E. C. Halbert, Nucl. Phys. 50, 353 (1964).
34. R. M. Eisberg and C. E. Porter, Rev. Mod. Phys. 33, 190 (1961).
35. C. M. Perez and F. G. Perey, Phys. Rev. 134, B353 (1964).

36. Nuclear Data Sheets (National Academy of Sciences, National Research Council, Washington, D. C.); B. Elbek, G. Igo, F. S. Stephens, Jr., and R. M. Diamond; in Proceedings of the Second Conference on Reactions between Complex Nuclei (John Wiley and Sons, New York, 1960), p. 107; A. H. Muir, Jr., and F. Boehm, Phys. Rev. 122, 1564 (1961).

37. D. E. Damouth, L. W. Jones, and M. L. Perl, Phys. Rev. Letters 11, 286 (1963).

38. J. A. Helland, Differential Cross Sections for Elastic Scattering of Positive Pi-Mesons on Protons in the Energy Region 50 to 100 MeV (unpublished Ph. D. Thesis), Lawrence Radiation Laboratory Report UCRL-10378, August 15, 1962.

39. M. Chretien, J. Leitner, N. P. Samios, M. Schwartz, and J. Steinberger, Phys. Rev. 108, 383 (1957).

40. J. Alitti, J. P. Barton, A. Berthelot, Nuovo Cimento 29, 515 (1963).

41. V. Cook, B. Cork, W. R. Holly, and M. L. Perl, Phys. Rev. 130, 762 (1963).

42. L. M. Simmons, Phys. Rev. Letters 12, 229 (1964).

43. M. L. Perl and M. C. Corey, Phys. Rev. 136, B787 (1964).

This report was prepared as an account of Government sponsored work. Neither the United States, nor the Commission, nor any person acting on behalf of the Commission:

A. Makes any warranty or representation, expressed or implied, with respect to the accuracy, completeness, or usefulness of the information contained in this report, or that the use of any information, apparatus, method, or process disclosed in this report may not infringe privately owned rights; or

B. Assumes any liabilities with respect to the use of, or for damages resulting from the use of any information, apparatus, method, or process disclosed in this report.

As used in the above, "person acting on behalf of the Commission" includes any employee or contractor of the Commission, or employee of such contractor, to the extent that such employee or contractor of the Commission, or employee of such contractor prepares, disseminates, or provides access to, any information pursuant to his employment or contract with the Commission, or his employment with such contractor.